The Astrophysical Journal, 986:52 (24pp), 2025 June 10 https://doi.org/10.3847/1538-4357/adc9ae

Increased Lyα Opacity in White Dwarf Photospheres from Transient H^- Resonances

Thomas A. Gomez[1,2,3,4,9], Mark C. Zammit[5], Jackson R. White[4,5], Evgeny Stambulchik[6], Ivan Hubeny[7], Igor Bray[8], Christopher J. Fontes[5], Michael H. Montgomery[4], Bart H. Dunlap[4], and Donald E. Winget[4]
[1] Department of Astrophysical and Planetary Sciences, University of Colorado Boulder, Boulder, CO 80305, USA; thomas.gomez@colorado.edu
[2] Laboratory for Atmospheric and Space Physics, University of Colorado Boulder, Boulder, CO 80303, USA
[3] National Solar Observatory, University of Colorado Boulder, Boulder, CO 80303, USA
[4] Department of Astronomy, University of Texas at Austin, Austin, TX 78712, USA
[5] Los Alamos National Laboratory, Los Alamos, NM 87545, USA
[6] Faculty of Physics, Weizmann Institute of Science, Rehovot 7610001, Israel
[7] Department of Astronomy, University of Arizona, Tuscon, AZ 85721, USA
[8] Curtin Institute, Department of Physics and Astronomy, Perth, Western Australia 6845, Australia
Received 2025 January 27; revised 2025 April 2; accepted 2025 April 5; published 2025 June 5

Abstract

The structure and emergent flux of hydrogen atmosphere white dwarfs depend on the opacity of the Lyα and Lyβ spectral lines. The opacity here is set by the strength and broadening of these lines; the latter is dictated by the far line wing, which is in the "quasi-static" limit of electron broadening, placing it in the incomplete collision regime, and describes the transient parts of electron and ion collisions. These transient stages of the collision form resonances: In the case of ions, they manifest as molecular resonances, while for electrons they are H^- resonances, both of which can only be captured quantum-mechanically. Quantum-mechanical calculations have historically preserved only a handful of broadening terms that are most important near the center of the line. However, in the wings of the line, the previously neglected terms that describe the transient stages of the collision need to be included. This requirement arises because, in the line wings, the broadening from the 1s ground state, which is generally assumed to be extremely small compared to the broadening of the upper state, is no longer negligible within a quantum-mechanical model that takes into account exchange interactions. The inclusion of all the transient terms results in asymmetries and extra broadening. The increased broadening of Lyα increases the opacity at the energy where most of the flux leaves the star. The broader Lyα lines also impact the visible flux, raising it by an amount that exceeds previously estimated errors.

Unified Astronomy Thesaurus concepts: Stellar spectral lines (1630); Atomic physics (2063); Collision physics (2065); Atomic spectroscopy (2099); DA stars (348); White dwarf stars (1799)

1. Introduction

White dwarfs (WDs) represent the final evolutionary stage of most stars (>97%) in our Universe (H. M. Van Horn 2015). These stars are important for many investigations in astronomy, including the initial–final mass relation (e.g., J. S. Kalirai et al. 2008; K. A. Williams et al. 2009), cosmochronology (D. E. Winget et al. 1987; G. Fontaine et al. 2001), and exoplanetary interior compositions (M. Jura 2003; B. Zuckerman et al. 2007). In addition, WDs can be used as physics laboratories for studying exotic processes such as crystallization (e.g., H. M. van Horn 1968; P.-E. Tremblay et al. 2019), as well as neutrino (D. E. Winget et al. 2004) and axion (e.g., A. Bischoff-Kim et al. 2008) emission. Due to their simple spectra, hot WDs are also used to calibrate major observatories and instruments, such as the Hubble Space Telescope (HST; G. Narayan et al. 2019; R. C. Bohlin et al. 2020) and the James Webb Space Telescope (K. D. Gordon et al. 2022). For HST, the quoted error estimates, which rely on model atmospheres, are under 1%. However, their astrophysical usefulness depends on our ability to infer accurate stellar masses and temperatures, while their usefulness as calibration sources depends on accurate calculations of their emergent flux distribution.

There are known problems when it comes to modeling UV and visible WD spectra. S. Sahu et al. (2023) discuss how the effective temperature of UV spectra (measured from the Cosmic Origins Spectrograph, hereafter COS, on HST) is systematically lower by a few percent than temperatures obtained via visible spectroscopy and photometry. This offset also translates to the derived masses, where masses derived from UV spectra were $\approx 0.052 \pm 0.005 M_\odot$ lower than spectroscopic masses and $\approx 0.024 \pm 0.003 M_\odot$ lower than photometric masses. Given that the mean mass of WDs is $\sim 0.6\,M_\odot$, these discrepancies translate into typical mass errors of 9% and 4%, respectively. The problem presented by S. Sahu et al. (2023) motivates a reexamination of the line broadening.

1.1. Sensitivity of Atmosphere Models to Lyα Opacity

For WDs with temperatures below $\lesssim$25,000 K and greater than $\gtrsim$9000 K, most of the radiation flux emerges around the Lyman series. The Lyα line is one of the strongest opacity sources in the spectrum. For cooler WDs below $\lesssim$9000 K, the peak flux of the star moves out of the Lyman series to longer wavelengths. Nevertheless, the Lyα red wing is still a dominant opacity source (D. Saumon et al. 2022). It is for this reason that this work focuses on the Lyα line specifically.

The structure of atmosphere models will, therefore, be sensitive to the calculated opacity of Lyα, which is determined,

[9] George Ellery Hale Fellow.

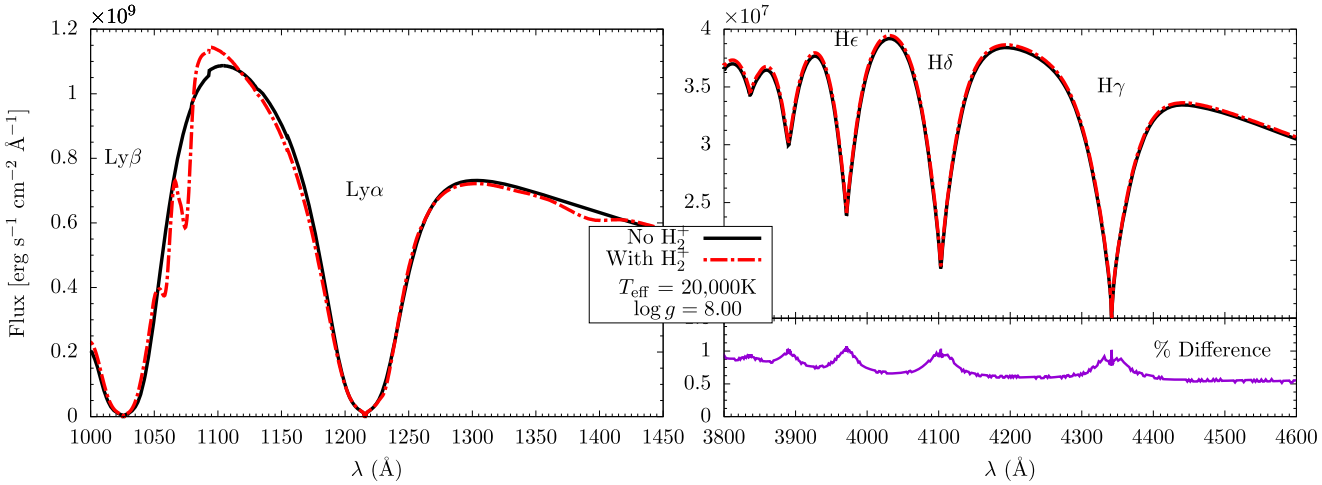

Figure 1. Demonstration of the impact on white dwarf spectra by including the H_2^+ resonances in the spectral line shapes. The H_2^+ resonances not only appear in the UV, but the increased opacity also causes a redistribution of flux down to the visible range. The resulting increase in the visible flux is between 0.5%–1.0%, which is a systematic change that is of order of the error estimated by G. Narayan et al. (2019) and R. C. Bohlin et al. (2020). Even though these resonances are 10^5–10^6 times weaker than the core intensity, these details are required for accurate atmosphere structure. Further, the line shapes in the emergent spectrum have changed.

specifically, by the strength and broadening of the line. The strength is largely dominated by the temperature, and non–local thermodynamic equilibrium corrections do not significantly impact this quantity. Therefore, our focus will be on the line broadening. We present a relevant demonstration in Figure 1 where the added opacity from the H_2^+ resonances (calculated by N. F. Allard et al. 1999) increases the flux in the visible range. This effect has been previously recognized by P. E. Tremblay & P. Bergeron (2009), who stated that the Lyman opacity "also affects the thermodynamic structure of the atmosphere." This is because an increased opacity in the region of high flux (UV) causes the so-called back-warming, that is an increased local temperature in the deep layers where the visible flux is formed, and thus to increase flux in this region. The other way to explain it is that an increased opacity in the UV leads to a decreased flux in this region, so in order to keep the total flux constant, it must be increased elsewhere, in this case the optical and IR regions. However, while the changes in the opacity in Lyα are important for the profile of the line itself, it is relatively minor when looking at the whole UV spectrum. Therefore, the resulting back-warming effect, and the increase of the flux in the optical range, is small. For a detailed discussion, refer to, e.g., I. Hubeny & D. Mihalas (2014, Section 17.6 and 18.5). This same effect was found by T. A. Gomez et al. (2021), where increased broadening from new quantum-mechanical line-shape calculations resulted in a change in the atmosphere structure and a change in the predicted flux distribution, emphasizing that the atmosphere structure of a WD is sensitive to the wing opacity of the Lyman lines.

A change in the model flux distribution of WDs from the UV to the visible will affect many different aspects of astronomy. The first would be the impact on HST calibrations, as mentioned above. The second would be on the determination of WD temperatures and masses, both spectroscopically and photometrically. Changes in our ability to determine WD masses affect our understanding of late-stage stellar evolution as well as cosmochronology. Lastly, we want to mention the impact that changing WD fluxes has on interstellar medium (ISM) research. WDs are used as background sources to determine the structure and chemical abundances of the ISM (e.g., J. Dupuis et al. 1995; N. Lehner et al. 2003; B. E. Wood et al. 2005), and changing the model flux distribution could change the determined abundances.

Due to all of these applications, it is therefore imperative that the broadening of the low n Lyman transitions (i.e., Lyα and Lyβ) is accurate for atmosphere structure calculations. And, by extension, accurate Lyα line shapes are necessary in order to accurately model (and interpret) both the UV and visible spectra of WDs. The importance of Lyα red-wing opacity in cool WDs (e.g., L. Frommhold 1993; P. M. Kowalski & D. Saumon 2006; D. Saumon et al. 2014) has been well established. However, there has not been the same attention given to the broadening of Lyα in hotter WDs. Therefore, a reexamination of Lyα in hotter WDs is warranted.

1.2. Different Approaches to Line-shape Calculations and Uncertainties in Lyα

It is important to point out that, unfortunately, there is significant disagreement between different line-shape codes for Lyα. This stems largely from the different approaches to line-shape calculations and the various approximations used, which are valid in some regimes but not others. The first models developed are "semianalytic," meaning that they rely on mathematical manipulation of the broadening equations to simplify the problem and calculate a line shape. Calculations such as P. Kepple & H. R. Griem (1968) or C. R. Vidal et al. (1973) are semianalytic. There are a wide variety of approximations used in semianalytical codes. Simulation methods arose by the 1980s that, using Monte Carlo methods, simulated the plasma conditions around the radiating atom, then performed an ensemble average of all the randomly generated plasma conditions. Such code include SIMU (E. Stambulchik & Y. Maron 2006) and XENOMORPH (T. A. Gomez et al. 2016; P. B. Cho et al. 2022). The number of approximations in simulation methods are far fewer than in semianalytic calculations. We elaborate more on the techniques used in line-shape calculations as well as their various approximations in Section 3.

In his report on the first Spectral Line Shapes in Plasmas Code Comparison Workshop (SLSP 2024), E. Stambulchik (2013) pointed out that one of the most interesting results was the large spread in the predicted widths (such as the full width

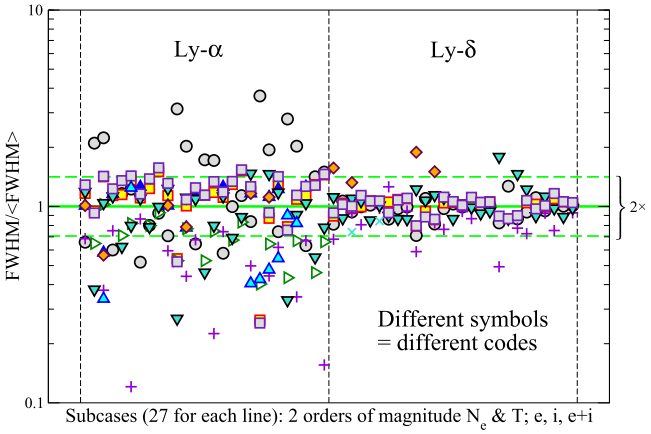

Figure 2. Comparison of Lyα and Lyδ widths calculated by different models. There are nine sets of plasma parameters (electron number density, n_e, and temperature, T, each spanning 2 orders of magnitude) with three variants of plasma composition (electrons, ions, or electrons and ions together, labeled as "*e*," "*i*," and "*e+i*," respectively). Each x-axis point corresponds to a different case. The y-axis is the ratio of the FWHM from a single calculation to the average FWHM (denoted by ⟨FWHM⟩) of all models submitted for that case. Different symbols correspond to different models. This figure was adapted from E. Stambulchik (2013).

at half-maximum, FWHM) for Lyα; the Lyδ line, which involves a larger basis set, did not show the same scatter. Figure 2 shows the scatter between Lyα and Lyδ from the first SLSP. Interestingly, but not surprisingly, the simulation codes (not present for the comparison in Figure 2) give consistent line widths among themselves. This agreement is largely due to the simulation codes using the same physics and solving the same equations with many of the same physical approximations. The only differences between the simulation codes have been (up until recently) in the numerical implementation of the integration of the time-dependent Schrödinger equation and the Fourier transform. The former was demonstrated to be inconsequential in the third SLSP (J. Rosato 2017), and the latter was found to only influence the numerical noise of the simulations (J. Rosato et al. 2020). Consistency between different simulation codes is a wonderful (and maybe a little surprising) result, although it is no guarantee of accuracy or that all the relevant physics has been captured.

The scatter seen in Figure 2 comes from a variety of sources, including the disparate electron broadening and ion dynamics treatments. Both of these effects are more important in Lyα than they are in other transitions (like Lyβ or Hβ) because it is a narrow line with an unshifted central component. For lines with an unshifted central component, the width is dominated by electron broadening and ion dynamics.

1.3. Experiments to Benchmark Lyα Line-shape Calculations

An important question is, "How do we know which line-shape models are correct?" Line-shape codes should, ideally, be verified through experiments. The Vidal–Cooper–Smith (VCS) theory (C. R. Vidal et al. 1973; M. Lemke 1997) has been benchmarked against the W. L. Wiese et al. (1972) experiment—in the visible. Of course, just because one theory performs well for the Balmer series is not a guarantee that its accuracy extends to Lyman lines.

There are few experiments dedicated to measuring the hydrogen Lyman lines; in general, measurements of UV spectral lines pose difficulties for instruments. Lyman lines are inherently difficult to measure due to how saturated the lines are (just like in a WD atmosphere). Saturated spectral lines are required to observe features far down in the line wings. For example, J. F. Kielkopf & N. F. Allard (1998) and J. F. Kielkopf et al. (2004) conducted experiments to measure the red wing of Lyα and Lyβ, respectively, and identified the presence of the unbound molecular resonances. This discovery makes it difficult to disentangle the population of the 1s ground state and the broadening of the spectral line. As a result, J. F. Kielkopf & N. F. Allard (1998) and J. F. Kielkopf et al. (2004) could not make any definitive conclusion about the quality of the line shape outside of confirming the existence of these resonant features.

This situation requires some elaboration. In the line core, it is easy to determine whether or not there is additional broadening, i.e., the width of the line has changed. However, in the line wings, that behavior is not present. Additional broadening in the wings can be (mostly) replicated by simply multiplying the opacity by a factor. Therefore, since both additional broadening and the populations increase the opacity of line wings by a multiplicative factor, it is incredibly difficult to isolate the impact of each on the opacity.

Independent diagnostics (such as photon Doppler velocimetry or optical Thomson scattering) are difficult to perform. Without accurate diagnostics, only self-consistency can be checked. In the case of the W. L. Wiese et al. (1972) experiments, the assumption of partial LTE was made, then the line-to-continuum ratio was used to obtain the temperature and density.

The Lyman lines are saturated for most WD temperatures, thus making the details of the line shape near the core of the line unimportant. The wings, by contrast, become far more important for dictating the opacity. The far line wings for hot WDs ($T_{\rm eff} \gtrsim 10{,}000$ K) are dominated by perturbations from electrons and protons, which are in the so-called "quasi-static" regime, where close collisions tend to be important. This situation is contrasted to the line core, which is dominated by long-range electron collisions and ion dynamics.

1.4. The Vidal–Cooper–Smith Theory

The "industry standard" line-shape calculations are based on the VCS model. The VCS theory is based on the so-called "unified theory," which unites the one-electron limit in the wings with the impact limit in the core, giving broad accuracy over a wide wavelength range. Unified theory calculations, as well as any other calculations that consider the time dependence of the interaction, better reproduce the measured wing behavior of spectral lines. The W. L. Wiese et al. (1972) experiment demonstrated the improvement of VCS over the P. Kepple & H. R. Griem (1968) profiles, which did not include the time dependence of the problem. VCS calculations compare well (as will be demonstrated in this work) with simulation codes such as SIMU (E. Stambulchik & Y. Maron 2006) and Xenomorph (T. A. Gomez et al. 2016; P. B. Cho et al. 2022), which make fewer approximations than the VCS work.[10] However, as pointed out by T. A. Gomez et al. (2022), these calculations rely on the semiclassical approximation, which treats the plasma particles as classical quasiparticles that obey

[10] VCS does not include time-ordering, but simulations implicitly include time-ordering. VCS also makes the binary-collision approximation, only taking account of two-body interactions, whereas simulations automatically include N-body interactions.

Newtonian mechanics. It has since been pointed out by T. A. Gomez et al. (2021) that the broadening of Lyα may be enhanced when the plasma electrons are treated quantum-mechanically.

The VCS calculation employs a further approximation that limits its accuracy: the dipole approximation. In this approximation, the dipole moment of the atomic transition interacts with the fluctuating electric field of the plasma. This choice results in accurate results near the line center in H I transitions, but will break down in the line wings (T. A. Gomez et al. 2024), where only a full-Coulomb treatment will produce a resonant structure from different states of the atom, e.g., H_2^+, and H^-. In principle, there could be many resonances that arise from H_2, H_3^+, H^{-2}, H_2^-, etc., but the probability of resonances arising from three or more body interactions is much smaller than from resonances arising from two-body interactions.

1.5. Resonant Structure in Line Shapes

When plasma particles come close to the radiating atom, they can induce a change in the charge state or molecular state. The plasma particles can collisionally ionize an atom, but the reverse process, in which electrons can be captured, is also possible (T. A. Gomez et al. 2020). Additionally, close-range ion collisions can form molecular-like electronic structures, such as H_2^+ (e.g., N. F. Allard et al. 1999). These changes in charge or molecular state often manifest as resonant structures in the line wings.

These resonances are 10^5–10^6 times weaker than the core intensity. Yet, they are clearly visible in WD spectra due to the lines being saturated, as demonstrated in Figure 1. Not only do they appear in the UV, but the additional opacity creates a line blanketing effect that redistributes flux to the visible, slightly raising the overall intensity of the visible spectrum and changing the emergent spectral line shapes. This redistribution of flux also occurs if the electron broadening is modified (T. A. Gomez et al. 2021). We point out that fitting model line spectra is a common tool to determine log g and mass of WDs (e.g., P. Bergeron et al. 1992), and modifying the flux distribution will modify those fits.

To create the unbound molecular resonances (e.g., H_2^+ resonances due to proton collisions) within the usual line-shape calculational framework (e.g., E. Stambulchik & Y. Maron 2006; T. A. Gomez et al. 2021), an ion full-Coulomb interaction is required (T. A. Gomez et al. 2024), although, in order for the calculation to predict the correct location of the resonance, the two-center H_2^+ problem must be solved. The BALROG code does not have this capability, so we rely on the unified theory (N. F. Allard et al. 1999) to account for ion resonances in this work.

The analogous resonant structure for electron broadening would be the formation of H^- resonances. Classical full-Coulomb calculations, such as E. Stambulchik & C. A. Iglesias (2022), cannot accurately reproduce the H^- structure. The BALROG code (T. A. Gomez et al. 2021) is capable of producing these H^- features. BALROG is distinct from other dedicated line-shape calculations because it treats the plasma electrons quantum-mechanically (allowing for the formation of H^-), uses full-Coulomb and exchange interactions, and solves the T-matrices exactly. The exact solution of the T-matrices is necessary for the calculation of H^- resonances; approximate solutions will *not* produce any H^- features. This capability is not remarkable, as there are collision codes that already do exactly this (e.g., I. Bray & A. T. Stelbovics 1992). In fact, collision codes that do these calculations have been used to calculate widths of isolated lines (H. R. Griem et al. 1997). However, calculations that use collision cross sections to calculate line widths are limited to the impact approximation. BALROG is therefore notable in its ability to go beyond the impact approximation and include the time dependence of the electron–atom collision. In the original work of T. A. Gomez et al. (2021), the BALROG Lyα line shapes were broader than VCS across the entire profile, which led to flux redistribution in the DA WD spectrum. One of the factors that contributed to the broader line shape was the presence of H^- resonances in the line wing that increased the opacity. The resulting flux was larger in the visible range than was predicted using VCS calculations by an amount that exceeded the estimated error in the flux calibrations (G. Narayan et al. 2019; R. C. Bohlin et al. 2020).

The T. A. Gomez et al. (2021) results demonstrated the importance of electron broadening of Lyα for WD spectroscopy in a way that had not been considered before. Therefore, due to the sensitivity of the atmospheric structure and the emergent flux to this broadening mechanism, it is imperative that our calculations be as accurate as possible.

1.6. Necessary Improvements in Quantal Calculations

The BALROG calculations previously presented in T. A. Gomez et al. (2021) were of limited accuracy since the lower-state and correlation broadening was neglected—a commonly used approximation for K-shell transitions that was also used by VCS. In this paper, we examine the importance of the $1s$ broadening and its correlation with the upper state, especially in the line wings. As we will demonstrate here, the broadening of the $1s$ ground state is not as negligible as previously thought.

Currently, BALROG includes the usual upper-state, lower-state, and correlation broadening terms. However, there are additional terms to the broadening operator that capture the transient stages of the collision that this paper will examine. Since the lower-state and correlation terms will not be negligible here, we must also consider these transient terms in the calculation of the Lyα profile wings. These transient terms are completely left out of the impact theory but are, in principle, included implicitly in VCS and simulation codes. The part that is new here, therefore, is the time dependence of quantum electrons rather than classical ones and, as discussed above, the temporary formation of H^- states, both the excited autoionizing states and the stable $1s^2$ ground state.

The rest of the paper is organized as follows. Section 2 outlines some important principles about line broadening, in particular the broadening of line wings, and discusses the transient collision phenomena. This is followed by a review in Section 3 of a number of approximations made in line-shape calculations of K-shell transitions. In Section 3.2, we make the same approximations as the standard VCS calculations to establish equivalency between calculations. Section 4 explores the validity of these approximations, focusing in particular on the classical approximation, demonstrating that quantum calculations result in larger cross sections for the ground state, and H^- resonances appear and manifest as additional broadening in the line wings. We also explore the necessity of having a larger basis set when performing these calculations as they increase broadening in the wings and cause interference

between different transitions. Section 5 includes the transient terms of the collisions within a quantum-mechanical framework, then explores the impact that they have on the line-wing opacity. In Section 6, we compare these new spectral line shapes against VCS and the simulation code SIMU. Finally, Section 7 shows the impact that these new profiles have on WD spectra. We wrap up with our conclusions and future outlook.

2. Transient Stages of Electron Broadening

This work focuses on electron collisional broadening. As discussed above, the molecular resonances that arise in ion broadening have already been examined by N. F. Allard et al. (1999). And while there are still improvements that can be made in ion broadening, the analogous treatment of electron collisions has yet to be examined.

The line shape is defined as the real part of the Fourier transform of the dipole autocorrelation function (M. Baranger 1958a; U. Fano 1963),

$$I(\omega) = \frac{\Re}{\pi}\int_0^\infty e^{i\omega t}\mathrm{Tr}\{\boldsymbol{D}\cdot\boldsymbol{D}(t)\rho\}\,dt, \tag{1}$$

where ω is the frequency of radiation, ρ is the density matrix that describes the population of atomic and plasma states, and $\boldsymbol{D}$ operates only on the atomic subspace. The dipole time evolution is defined in the Heisenberg picture as

$$\boldsymbol{D}(t) = e^{iHt}\boldsymbol{D}e^{-iHt}. \tag{2}$$

The time evolution operators, $\exp(-iHt)$, span the space of both the atom and the plasma bath in which it is embedded. When averaged over a large number of plasma perturbations, the autocorrelation function decays to zero at long times. The relaxation time is a characteristic time that is required for the autocorrelation function to decay. The relaxation time is inversely proportional to the width of the spectral line, $\Delta\omega$.

It has been well established that electron collisions with a radiating atom are the driving mechanism behind electron broadening (M. Baranger 1958a). In his seminal work, M. Baranger (1958a) established that the Lorentzian width of a line—in the impact approximation—is closely related to the collision T-matrix (or the scattering S-matrix in an alternate representation). Appendix A has a full discussion about the T-matrix and its properties. The T-matrix is proportional to the collision amplitude,

$$\langle a\boldsymbol{k}|T|a'\boldsymbol{k}'\rangle \propto f(\theta,\phi), \tag{3}$$

where a, a' denote atomic states, $\boldsymbol{k}$ and $\boldsymbol{k}'$ are the momenta of the projectile electron, and lastly θ and ϕ denote the scattering angles. Through the optical theorem (M. Baranger 1958a), the collision amplitude can be written in terms of the total cross section:

$$\Im f(0) = \frac{k}{4\pi}\sigma_T. \tag{4}$$

We point out that collisions have a certain timescale associated with them. The collision timescale is *not* the same as the relaxation timescale described above for the line shape. The line width can be written in terms of the total collision cross section (i.e., the sum over all collision channels). The width is, however, *not* simply the addition of the contributions of upper and lower states, but, rather, there is a cancellation of elastic terms. M. Baranger (1958a) therefore writes the width for an isolated line as

$$w = \left\{\frac{1}{2}n_e v\left[\sigma_u^{(\mathrm{inel})} + \sigma_l^{(\mathrm{inel})} + \int d\Omega|f_u(\Omega) - f_l(\Omega)|^2\right]\right\}_{Av}, \tag{5}$$

where the first two terms in brackets are the total inelastic cross sections of the upper (u) and lower (l) states, respectively, and the last term is the elastic contribution, which has some notable cancellation, as demonstrated in the isolated line case (H. R. Griem et al. 1997). Due to the Lorentzian shape of electron broadening, it is clear how one can interpret the broadening as being a result of collisions shortening the lifetime of the atomic states.

When one explores the microphysics of electron broadening, it is clear that the mechanism for electron broadening is more complicated than this simple description of the shortening of the lifetime of the atomic state. Rather, each electron collision constitutes an interruption of the time evolution of the state, amounting to a sudden phase shift. Further, each collision could knock the atomic electron into a different state, leading to memory loss (S. Alexiou 2009). After performing an ensemble average over all of these processes and different combinations of collisions, the resulting average-time evolution is roughly a decaying exponential that, when Fourier transformed, results in a Lorentzian line shape.

The last term in Equation (5)—often referred to as the "interference term" (M. Baranger 1958a; U. Fano 1963; H. R. Griem et al. 1997), but we will refer to this as the "correlation correction"—is extremely important and is necessary for the calculation of accurate line shapes. U. Fano (1963) explains the presence of this term more fully, stating that, when an atom is radiating, the elastic collisions between the upper and lower states do *not* "constitute a pair of distinguishable, mutually exclusive events." Further, if the upper and lower states are perturbed in the same way, then the energy levels would shift in tandem, resulting in no interruption of radiation, and there would be no broadening. In other words, Fano states that it "would cancel out completely the contribution of elastic scattering to the line width if they happened to be equal because in this event elastic scattering would not perturb the molecular radiation process at all." Another way to think of this term is to correct for the fact that the upper- and lower-state time evolutions are not independent of each other. We point out that semianalytic codes have to explicitly include the correlation correction; simulation codes generally include this effect automatically.

It is important to note that M. Baranger (1958a) makes the impact approximation, which makes the assumption of completed collisions. E. W. Smith et al. (1969) states that the completed assumption implies that "any collision which occurs during the time of interest can be completed during that time." We point out that, often, the timescale of relevance is the relaxation time of Equation (1), not the collision time. This result allows the replacement of the time evolution operator with the S-matrix since the S-matrix is defined in terms of the infinite-time limit (B. A. Lippmann & J. Schwinger 1950). The impact approximation, therefore, treats the entire frequency range of the line shape as a generalized Lorentzian. We know empirically from experiments, such as W. L. Wiese et al. (1972), that this is not correct. The explanation for the

deviation from Lorentzian line shape in the wings is attributed to the time dependence of the broadening problem.

Fano's derivation includes the time dependence of the electron collisions, and thus, the broadening is dependent on the frequency of the photon, being a generalized form of Equation (5). This formalism has become the basis for the E. W. Smith et al. (1969; and later C. R. Vidal et al. 1973, i.e., VCS) calculations that are so widely used in WD atmospheres. Fano's expression includes several additional terms not present in Equation (5), which he describes as being entirely the result of transient stages of the collisions. These terms are generally neglected because their contribution vanishes entirely at the line center. We will refer to these additional terms as

$$M_{\text{transient}}(\omega), \tag{6}$$

which is the focus of this work. M. Baranger (1958a) did not consider these types of collisions, and, therefore, they were not included within his formalism.

It is extremely common to Taylor-expand the electron-broadening operator. However, when this is done, most of the terms contained in $M_{\text{transient}}(\omega)$ are not included in the final formulation. The work that was based on the relaxation theory, such as the work carried out at the University of Florida (e.g., J. T. O'Brien & C. F. J. Hooper 1974; R. J. Tighe & C. F. J. Hooper 1976; L. A. Woltz & C. F. J. Hooper 1984; D. P. Kilcrease et al. 1993), as well as other more recent work like T. A. Gomez et al. (2018), Taylor-expand Fano's formula to the second order in the atom–plasma interaction. As a result, only all-order calculations would be able to capture this effect. Until recently, the only all-order calculations were semiclassical, which assumes that plasma particles are classical quasiparticles. The VCS and simulation codes (e.g., M. A. Gigosos & V. Cardenoso 1987; E. Stambulchik & Y. Maron 2006) are effectively all-order methods.

T. A. Gomez et al. (2021) extended the all-order capabilities to a calculation that treats the plasma electron quantum-mechanically. However, only the frequency-dependent version of Baranger's formula was used, and $M_{\text{transient}}(\omega)$ was not included. Since the focus of T. A. Gomez et al. (2021) was as a diagnostic, such as that found in laboratory settings, it was reasonable to omit $M_{\text{transient}}(\omega)$ because those terms do not contribute to the line center.

As a last point of intuition, we point out that the line wings are dominated by short-range collisions, which create strong perturbations. Each interaction between a plasma particle and the atom shifts the energy levels, and weak interactions simply do not shift energy levels to the same degree that strong interactions do. The decay of the autocorrelation function (Equation (1)) is dictated by the accumulation of weak collisions over the relaxation time. Since only small detunings ($\Delta\omega$) sample long timescales, it follows that the weak collisions impact the core of the line more than the wings. And lastly, as the density increases, strong collisions become more common, and the line width becomes larger.

As a side note, as the energy levels of the atom become nondegenerate, the broadening will increasingly become dependent on strong collisions, which are the most effective mechanism for driving inelastic collisions. In fact, this scenario becomes so typical that screening of the atom–plasma interactions becomes less important for isolated lines than it does for hydrogenic lines.

As stated in the introduction, in order to calculate accurate WD spectra, the wing opacity of Lyα in particular needs to be accurate. Therefore, these transient terms that are usually omitted need to be included within the broadening formalism. One particular complication, as demonstrated by T. A. Gomez et al. (2021), is the presence of additional broadening in the line wings due to dielectronic capture, a phenomenon that is only a feature of all-order quantum-mechanical calculations. For neutral hydrogen, this effect means that H^- resonances impact the wing behavior of Lyα, creating an important opacity source. It is therefore the intent of this work to include these transient terms in the broadening and examine their importance in determining the opacity of WD photospheres.

3. Common Approximations for *K*-shell Line Shapes

Here, we discuss the different approximations commonly used in the calculation of hydrogen line shapes. Because the focus of this work is on electron broadening, ion dynamics (e.g., D. B. Boercker et al. 1987; M. A. Gigosos & V. Cardenoso 1987; A. Calisti et al. 1990; E. Stambulchik & Y. Maron 2006) will not be addressed.

There are a number of ways to calculate line shapes. The principal ones are through semianalytic and simulation methods. Other methods exist, such as the model-microfield method (e.g., C. Stehle & S. Jacquemot 1993), but we will not discuss them further. Semianalytic methods are usually based on one of the following electron-broadening theories: the impact theory (M. Baranger 1958a), relaxation theory (U. Fano 1963), or the kinetic theory (T. Hussey et al. 1975), each with their own approximations. Simulation methods generate a time-dependent fluctuating plasma potential by simulating classical quasiparticles, solve the time-dependent Schrödinger equation, and then repeat the process to properly sample the plasma statistics.

Of the approximations that will be discussed, we include the dipole approximation, the no-quenching approximation, the approximation that there is no lower-state broadening for *K*-shells, the semiclassical approximation, the impact approximation, and the single-perturber approximation. Some approximations, such as screening and the factorized density matrix, will not be discussed here because their use is ubiquitous and established (as for screening) or will be the subject of future exploration (factorized density matrix). Additionally, we also briefly mention the second-order approximation, which relies on a Born expansion for the collision problem whose accuracy breaks down for neutrals unless an appropriate strong-collision cutoff is employed in the calculations.

Dipole approximation. One of the most ubiquitous approximations in the field of line broadening is the use of the dipole interaction,

$$\begin{aligned} V_{\text{atom}-\text{plasma}} &\approx -\boldsymbol{D}_a \cdot \sum_p q_p \frac{\boldsymbol{r}_p}{|\boldsymbol{r}_p|^3} \\ &\approx -\boldsymbol{D}_a \cdot \boldsymbol{\varepsilon}_{\text{plasma}}, \end{aligned} \tag{7}$$

to describe the interaction between the atom and the perturbing plasma particles; this is what gives rise to the name "Stark broadening." A more physical description is to use the full-

Coulomb interaction,

$$V_{\text{atom}-\text{plasma}} = \sum_{ap} \frac{q_a q_p}{|\boldsymbol{r}_a - \boldsymbol{r}_p|} - \frac{q_p Z}{|\boldsymbol{r}_p|} = \sum_{ap} q_p \sum_k \left[\frac{r_<^k}{r_>^{k+1}} - \delta_{k,0} \frac{Z}{r_p} \right] \times (2k+1) P_k(\cos\gamma_{ap}), \quad (8)$$

where Z is the charge of the nucleus, $r_</r_>$ is the lesser/greater of r_a and r_p, k is the various multipoles of the potential (with $k = 1$ being the dipole term), $P_k(x)$ is a Legendre polynomial, and γ_{ap} is the angle between the atom and perturbing electron. The advantage of using the dipole approximation is that dipole moments are calculated by most atomic structure codes, making the relevant line-broadening data relatively easy to obtain. Contrast this with Equation (8), which requires more effort to calculate. Other multipoles, including the monopole and quadrupole terms, must also be calculated. To calculate the case for which the perturbing plasma electron is closer to the nucleus than the atomic electron, wave functions are needed; E. Stambulchik & C. A. Iglesias (2022) used analytic expressions to calculate this scenario for hydrogenic radiators. It is fair to say that spectral line shapes in a pressure-broadened environment are dominated by the Stark effect, and a treatment based on a complete Coulomb interaction instead of the dipole approximation will be a correction rather than a major change to the predicted line shapes.

We would like to emphasize that a full-Coulomb treatment is necessary for the creation of H^- resonances in the T-matrix solutions. Additionally, as we will emphasize in the section on quantum electrons, exchange interactions also need to be included in the calculations.

No-quenching approximation. For a hydrogenic transition, the "no-quenching" approximation means excluding Stark mixing between states with different n values. For example, for Hβ (a transition from $n = 2$ to $n = 4$), the $n = 3$, $n = 5$, etc. states would not be included in the calculation, nor would matrix elements between $n = 2$ and $n = 4$ be included. The resulting eigenvalue solutions for hydrogenic systems are linear as a function of the electric-field magnitude.

This is a common approximation that helps to speed up calculations. Calculations, such as those from P. Kepple & H. R. Griem (1968), E. W. Smith et al. (1969), and M. A. Gigosos & V. Cardenoso (1987), have employed this approximation. It is common knowledge that, at higher densities, the electric microfields in the plasma are much stronger, and the quadratic Stark effect becomes notable. The result is a well-known asymmetry in the spectral lines (e.g., S. Djurović et al. 2009). As with the dipole approximation, the no-quenching approximation tends to dominate the line shape, and any contributions from cross terms tend to be corrections rather than major changes to the line shape.

No-lower-state broadening. In semianalytic line-broadening calculations, the (frequency-dependent) electron-broadening operator is given in terms of thermally averaged T-matrices (see Appendix A for more information on our T-matrix calculations),

$$\langle ab|\mathcal{H}(\omega)|a'b'\rangle \approx n_e \lambda_T^3 \int_0 dk k^2 e^{-\beta E_k} \times \{\langle ak|T(E_b + E_k + \omega)|a'k\rangle \delta_{bb'} - \delta_{aa'} \langle bk|T^*(E_a + E_k - \omega)|b'k\rangle + i\pi \int dk' k'^2 \times [\delta(E_a + E_k - \omega - E_{b'} - E_{k'}) \times \langle ak|T(E_a + E_k)|a'k'\rangle \langle bk|T^*(E_{b'} + E_{k'})|b'k'\rangle + \delta(\omega - E_{a'} - E_{k'} + E_b + E_k) \times \langle ak|T(E_{a'} + E_{k'})|a'k'\rangle \langle bk|T^*(E_b + E_k)|b'k'\rangle]\}, \quad (9)$$

The dipole approximation is not physical near the origin of the atom due to the divergence of the r_p^{-2} behavior of the electric field. Further, for ionized radiators, a plasma polarization shift is present only in calculations with a full-Coulomb interaction (G. C. Junkel et al. 2000). The inclusion of this shift has had several successes in reproducing plasma measurements. For example, the full-Coulomb calculation of E. Stambulchik & C. A. Iglesias (2022) was able to fully explain the shifts of the Pα line of He^+ (F. Sobczuk et al. 2022; K. Dzierżęga et al. 2024), and the calculation of T. A. Gomez et al. (2021) was able to determine the true density of a solid-density Ti experiment (B. F. Kraus et al. 2021).

For neutral hydrogen, the difference between a dipole and full-Coulomb treatment was small enough to be of no consequence in the line core (T. A. Gomez et al. 2024), but it did make a difference in the line wings. The most noticeable difference was in the ion broadening, where the calculations approximated the unbound molecular resonances at incorrect wavelengths. Using a molecular basis set, as was done by N. F. Allard et al. (1999), is necessary to accurately predict the locations of these resonances.

where the set of a and b denote the upper and lower states, respectively, k denotes the perturbing electron states, E denotes the energy, λ_T is the thermal de Broglie wavelength, and $\beta = 1/k_B T$. We note that the expression in Equation (9) is only approximate under the single-perturber approximation and is valid near the line center. The right-hand side (RHS) of Equation (9) contains terms from the upper-state, lower-state, and two correlation correction terms. From this expression, it can be plainly seen that the electron broadening is determined by the collision T-matrix (M. Baranger 1958a; U. Fano 1963).

In K-shell transitions, the broadening of the upper state is generally much larger than the broadening of the ground state or the correlation correction. Therefore, it is common to approximate the line width of K-shell transitions as

$$\langle ab|\mathcal{H}(\omega)|a'b'\rangle \approx n_e \lambda_T^3 \int_0 dk k^2 e^{-\beta E_k} \times \langle ak|T(E_b + E_k + \omega)|a'k\rangle \delta_{bb'}. \quad (10)$$

The dominant broadening, as mentioned when discussing the no-quenching approximation, is from states of the same

principal quantum number. For K-shell transitions, there are no other states (of the same n) that the $1s$ electron can connect to. Therefore, the broadening from the lower state, $1s$, is quite insignificant compared to the broadening of any upper state—at least in the line core. We will show in this work that, in the line wings, the broadening of $1s$ and the correlation corrections are not negligible. Further, under the no-quenching and dipole approximations, the broadening of the $1s$ ground state is zero.

Semiclassical approximation. A common practice, dating back to some of the first practical line-shape calculations (H. R. Griem et al. 1959), is to assume that plasma particles obey the classical Newtonian dynamics rather than quantum mechanics. This is a rather standard approximation, and many calculations have shown a correspondence between the two methods (S. Alexiou & R. W. Lee 2006)—at least in the line cores.

This correspondence is remarkable, considering that classical calculations do not include the energy exchange between the colliding plasma electrons and the radiating atom. There is one physical effect that is worth mentioning here, which is that a quantum calculation will include dielectronic capture. Dielectronic capture was first included by T. A. Gomez et al. (2020) and included in a more exact formalism in T. A. Gomez et al. (2021). The result was the presence of H^- resonances in hydrogen T-matrix calculations. To be clear, these resonances are present in the collision cross sections used to calculate the electron-broadening operator and are *not* H^- transitions sometimes seen in cool WD spectra (N. F. Allard et al. 2004). These H^- resonances will become an important aspect of Lyα line-shape calculations.

There are a couple of other important factors involved with a quantum-mechanical calculation, the first being that a true quantum calculation will also take into account the indistinguishability of fermions. This concept requires the wave function of the atom plus a single perturber to have the property

$$\Psi(r_a, r_p) = (-1)^S \Psi(r_p, r_a), \tag{11}$$

where Ψ is the total wave function, r_a and r_p are the coordinates of the atom and perturbing electrons, respectively, and S is the total spin of the two-particle system. This antisymmetry with respect to the exchange of coordinates results in the exchange interaction (H. A. Bethe & E. E. Salpeter 1957).

The second important factor is a result of detailed balance. In quantum-mechanical calculations, there are exponential damping factors that appear, i.e.,

$$w(-|\Delta\omega|) = e^{-\beta|\Delta\omega|} w(|\Delta\omega|), \tag{12}$$

where w is a shorthand for the frequency-dependent width. This behavior is a result of detailed balance, which causes the far wing of one side of the profile or the other to decay faster than the other.

Impact approximation. The first line-shape formulations employed the impact theory (M. Baranger 1958a, 1958b, 1958c; A. C. Kolb & H. Griem 1958). The impact theory makes a number of approximations, including taking the long-time limit (giving line shapes their Lorentzian shape) and assuming that the collision time is less than the time between collisions (disentangling collisions). The latter assumption means that collisions are dominated by one perturbing electron at a time. As a consequence, the transient stages of collisions with plasma particles are ignored, and only completed collisions are considered, i.e., partial collisions are neglected.

It has been well established experimentally (W. L. Wiese et al. 1972) that, because the impact approximation neglects the time dependence of the collisions, the wings are inaccurate. For example, the results of P. Kepple & H. R. Griem (1968) compared well to line core measurements, but tended to overestimate the wings of the Balmer lines. Of the calculations compared, only VCS, which takes into account the time dependence of the problem, could accurately capture the wing behavior of the Balmer lines. This success helped to establish VCS as the industry standard for hydrogen line shapes in astrophysics research.

Single-perturber approximation. In nearly all semianalytic treatments of electron broadening, the broadening is reduced to solving the two-body problem in detail and then multiplying the entire function by the electron density (M. Baranger 1958a, 1958b, 1958c; P. Kepple & H. R. Griem 1968; E. W. Smith et al. 1969; C. R. Vidal et al. 1973; T. A. Gomez et al. 2021). This approximation is one of the foundational approximations in the impact theory. While not formally required in the relaxation (U. Fano 1963) or kinetic (T. Hussey et al. 1975) theories, any practical implementation of interactions involving more than just the atom plus one plasma electron is too computationally expensive for semianalytic methods.

This is one area where simulation methods (M. A. Gigosos & V. Cardenoso 1987; E. Stambulchik & Y. Maron 2006; P. B. Cho et al. 2022) excel. Multibody effects can be captured with little additional computational cost.

3.1. Additional Approximations

As mentioned above, there are a few other approximations that are worth discussing, but will not be examined in this work. These include screening, the second-order approximation, and the factorized density matrix approximation.

Screening. When the N-body behavior of the plasma is not included, screening potentials are used to account for the correlations between plasma particles. It is well established that, in the presence of a test charge, plasma particles will rearrange themselves, and their motion and positions become correlated. A fully interacting plasma solution takes these plasma correlations into account, as found by E. Stambulchik et al. (2007). However, many calculations involve simplifying assumptions, such as the single-particle/binary-collision approximation. Sometimes simulation codes use "trivial" molecular dynamics, where particles travel on straight paths around neutrals and hyperbolic trajectories (when a Coulomb field is assumed, but more general curves if the Debye screening is accounted for) around charged radiators. These simplifying procedures can account for the missing correlations by screening the atom–plasma interaction.

The justification for using screened potentials was developed formally by H. Capes & D. Voslamber (1972) and T. Hussey et al. (1975) using the BBGKY hierarchy. Within the kinetic-theory formalism, there were both static and dynamic screening contributions. To our knowledge, only T. W. Hussey et al. (1977) and D. B. Boercker & C. A. Iglesias (1984) evaluated the dynamic screening contribution, but they were evaluated under the second-order approximation. All other calculations have only used the static screening.

Here, our use of static screening is valid because we are only focused on the far line-wing behavior, which is in the static limit. The full screening (i.e., the inclusion of dynamic and static screening) results differ in changes in the line shape only for detunings less than the plasma frequency (T. W. Hussey et al. 1977),

$$\omega_p = \sqrt{\frac{4\pi n_e e^2}{m}}, \tag{13}$$

which is only about 0.01 eV in our calculations and can be ignored for the far wing. Further, in this approximation, consideration of the interaction with plasma oscillations (D. Bohm & E. P. Gross 1949a; D. Bohm & E. P. Gross 1949b) is assumed to be negligible (H. R. Griem 1974).

Second-order approximation. We want to make a note about the second-order approximation. This is a common approximation within analytic line-shape treatments that Taylor-expands the formula for the electron-broadening operator in powers of the interaction potential; simulations never make this approximation. This situation is akin to making the Born approximation in collision problems. The accuracy of the second-order approximation can be maintained with strong-collision cutoffs. Such cutoffs are absolutely necessary to compare well with measured spectra of neutral elements like H I (C. A. Iglesias 2016). Calculations such as P. Kepple & H. R. Griem (1968) or J. T. O'Brien & C. F. J. Hooper (1974) use the second-order approximation, but only the former study uses strong-collision cutoffs.

We speculate that one of the reasons for the scatter previously discussed in Figure 2 is the various strong-collision cutoffs used by different codes. This is a plausible explanation as some codes are tailored to certain conditions, and, therefore, their accuracy is not applicable to all conditions. For example, the cutoff procedures between P. Kepple & H. R. Griem (1968) and H. R. Griem et al. (1979) are different, with the latter applying to ions, and the former applying to neutral H. As an example of how important these strong-collision cutoffs are, T. Nagayama et al. (2016) compared line-shape models from several codes and found, even for the Heγ line of Mg^{10+}, the inferred density between two popular line-shape codes with different strong-collision prescriptions differing by about 50%.

One of the achievements of the VCS work (E. W. Smith et al. 1969) was that it is an "all-order" calculation, meaning that it does not employ the second-order approximation and does not require a strong-collision cutoff. For a long time, all-order treatments of electron broadening were relegated to semiclassical calculations that used the dipole approximation. Recently, T. A. Gomez et al. (2021) created the first all-order, quantum-mechanical, full-Coulomb electron-broadening calculation.

We will not explore the second-order approximation further within this work. All of the calculations that we will be comparing here are "all-order" or exact.

Factorized density matrix. To calculate the thermal averages necessary to produce line widths, a density matrix must be used to sample the appropriate variables of the perturbing electrons. The density matrix, defined in LTE to be

$$\rho = e^{-\beta \mathrm{H}}/\mathrm{Tr}\, e^{-\beta \mathrm{H}}, \tag{14}$$

should, in principle, include all terms of the Hamiltonian. However, one of the most common approximations is to ignore the interaction between systems. This choice allows the density matrix to be factorized into atomic and plasma components, i.e.,

$$\rho \approx \rho_a \rho_p. \tag{15}$$

Some effort has gone into exploring the consequences of including the atom–plasma correlations in the density matrix (T. Hussey et al. 1975; T. A. Gomez et al. 2018; C. A. Iglesias & T. A. Gomez 2024). The correlations result in an asymmetry of the profile beyond about

$$|\Delta\omega| \gtrsim T.$$

This behavior will, therefore, be consequential to the calculation of the Lyα opacity, but is beyond the scope of this work.

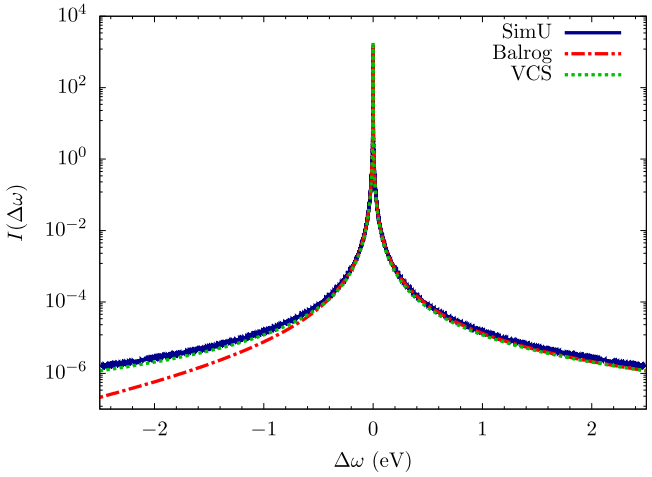

Figure 3. Comparison of SIMU, BALROG, and VCS results with the no-quenching approximation at $T_e = 1$ eV and $n_e = 10^{17} e$ cm^{-3}. The red wing of Balrog decreases faster than the others due to the detailed balance property seen in quantum calculations (Equation (12)). Otherwise, the agreement between the three calculations is superb.

3.2. Comparison of Simulation and Quantum Codes with VCS When Making the Same Approximations

The unified theory of VCS is a unification of the impact limit in the line center (dynamic limit) with the static limit in the wings. E. W. Smith et al. (1969) state that "the only essential difference between the impact theory and the unified theory is due to the fact that the unified theory does not make the completed collision assumption." This statement indicates that the VCS theory still employs the single-perturber approximation.

The VCS profiles that are tabulated (C. R. Vidal et al. 1973; M. Lemke 1997) make a number of other approximations. These include the dipole approximation, the classical approximation, the no-quenching approximation, the no-lower-state broadening approximation for *K*-shell transitions, and the factorized density matrix approximation. Another approximation made by VCS is the neglect of so-called "time-ordering" (L. J. Roszman 1975). Time-ordering adds additional broadening, especially in the core.

To test the correspondence between VCS and the more physically complete BALROG and SIMU models, we can make the same approximations as VCS within BALROG (as far as is possible) and SIMU, and compare these results to VCS. For example, if the no-quenching approximation is made, the wing

behavior of BALROG, SIMU, and VCS is nearly identical, as is seen in Figure 3. We note that, for this comparison, exchange interactions were not included in the BALROG calculation. Given the results presented in Figure 3, this would seem to confirm that, under the no-lower-state broadening approximation and the no-quenching approximation, the three different calculations give nearly identical electron-broadened shapes for the wings of Lyα. The only real deviation is that BALROG includes detailed balance, which causes the depression of the red wing.

We first compared the cores of the lines between the different calculations (not shown here). It is obvious that there are differences between VCS and BALROG (T. A. Gomez et al. 2021) in the core. This behavior was initially attributed to the difference between classical and quantum-mechanical calculations, especially considering that the difference vanished at higher temperatures, where the thermal de Broglie wavelength becomes smaller, and the plasma electrons become more classical. However, calculations from SIMU also show additional broadening in the core over VCS. We now attribute this difference to the lack of time-ordering included in VCS (L. J. Roszman 1975).

It is important to point out the different physics involved in the classical calculations (VCS, SIMU) and quantum calculations (BALROG). In a classical picture, the wing behavior is a result of the electrons approaching the static limit. This is not the case with the quantum calculation; rather, in the wing, energy is being transferred to (blue wing) or away from (red wing) the colliding electron. If we examine Equation (10), we can write the imaginary part of the electron-broadening operator as

$$\begin{aligned} &\Im\langle \alpha k|T(E_\alpha + E_k + \Delta\omega)|\alpha k\rangle \\ &= -\pi \int dk'' \sum_\alpha |\langle \alpha k|T(E_\alpha + E_k + \Delta\omega)|\alpha'' k''\rangle|^2 \\ &\quad \times \delta(E_\alpha + E_k + \Delta\omega - E_{\alpha''} - E_{k''}). \end{aligned} \tag{16}$$

The delta function ensures that the electron leaving the collision has the energy

$$E_{k''} = E_k + \Delta\omega \tag{17}$$

in the no-quenching approximation. It is clear from this expression that the outgoing electron will gain/lose energy in the blue/red wing of the profile. Therefore, the relationship between the red and blue parts is a Boltzmann factor, as already discussed and shown by Equation (12). This change of energy of the colliding electron will become important when the no-quenching approximation is removed. Given the vastly different physics involved, it is impressive that classical and quantum line-shape calculations agree as well as they do.

4. Exploration of Approximations and Calculational Considerations

In the next sections, we explore the various aspects of the above-mentioned approximations on the H Lyα line. As already stated above, there are some obvious approximations that do not warrant further discussion. In the following, we remove some of these approximations to examine their importance. We begin with removing the no-quenching approximation. Lifting this approximation is known to cause asymmetries (S. Djurović et al. 2009), so it is worth exploring. Next, we examine the quantum-mechanical nature of collisions with the 1s state of H. As we will show, when exchange interactions are included, lower-state

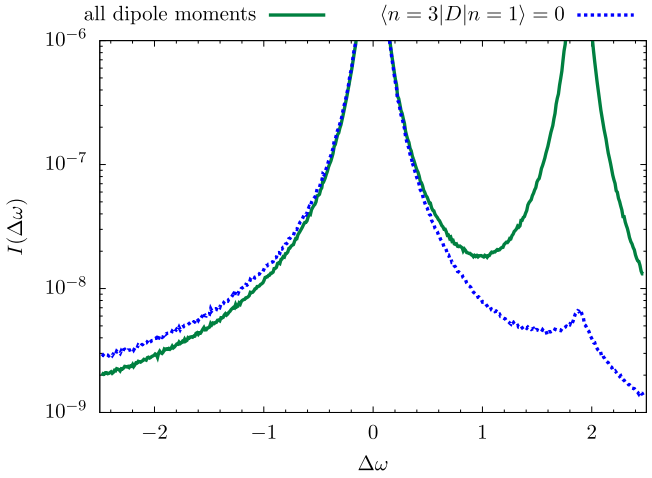

Figure 4. Comparison of SIMU calculations with and without Lyβ dipole matrix elements included; plasma conditions are the same as in Figure 3. Interaction matrix elements between $n = 2$ and $n = 3$ cause a bump in the Lyα blue wing at the location of Lyβ. This indicates that, at that photon energy, the mixing of $n = 2$ and $n = 3$ is stronger; these features were present in the XENOMORPH calculations of P. B. Cho et al. (2022). However, interference between Lyβ and Lyα causes the Lyα red wing to decrease slightly.

broadening and correlation terms become important in the wings. Historically, only a few correlation terms are included within semianalytic calculations. We therefore examine the importance of the additional terms that are usually included; U. Fano (1963) describes these terms as arising from the transient stages of collisions.

4.1. Interference between Different Transitions

One interesting aspect of the calculations is the interference between $n = 2$ and $n = 3$ transitions. Both SIMU (E. Stambulchik & Y. Maron 2006) and BALROG (T. A. Gomez et al. 2021) calculations produce this interference, which causes the red wing to be reduced slightly; Figure 4 demonstrates this effect using SIMU. From a theoretical perspective, this concept can be most effectively demonstrated using the formalism of BALROG. The line-shape calculation using the analytic theory requires the calculation of the broadening operator acting on the dipole matrix,

$$I(\omega) = \mathrm{Tr}\, DR(\omega)\rho D, \tag{18}$$

where

$$R(\omega) = \frac{1}{\omega - L_0 - \mathcal{H}(\omega)}. \tag{19}$$

In the most general case, $R(\omega)$ has elements that connect $n = 2$ to $n = 3$. Therefore, when performing this calculation, the cross terms in $R(\omega)$ will contribute to each individual line shape.

The resulting effect is a slight lowering of the red wing of Lyα line and a raising of the opacity between the lines. If we delete the $n = 3 \rightarrow 1$ matrix elements in D on the left-hand side of $R(\omega)$ in Equation (18), then the resulting line shapes display a resonance that is positive on the red side and negative on the blue side of Lyβ. When the Lyβ line is included, this slightly negative contribution creates an asymmetry in Lyβ. We note that this singularity is merely the result of trying to define a Lyα line when states of different n are mixed together. When all matrix elements of D are included in the calculation, no such singularity exists. For calculations in the remainder of the

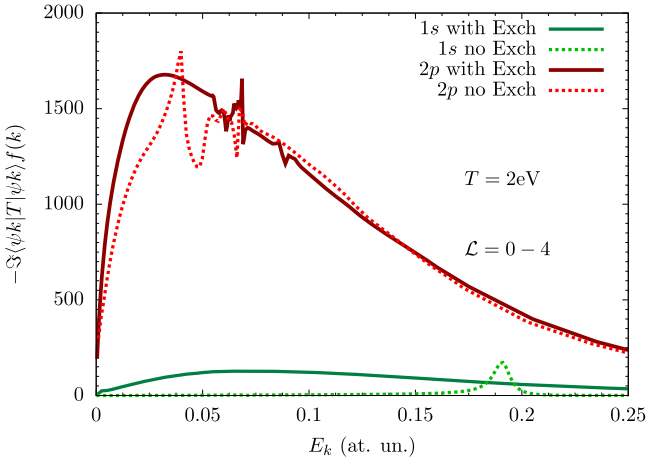

Figure 5. Comparison of fully on-shell T-matrix calculations for $2p$ (red) and $1s$ (green) with (solid lines) and without (dashed lines) exchange. Only partial waves up to $\mathcal{L} = 4$ are included in these calculations due to these waves containing the close collisions. Exchange is responsible for significant increases in the $1s$ elastic T-matrix.

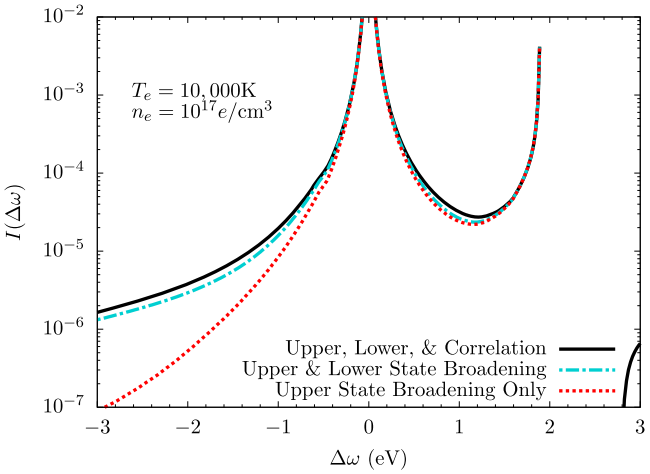

Figure 6. Plotted is the normalized intensity (Equation (1)) as a function of wavelength, a comparison of BALROG calculations with upper-state-only broadening (Equation (10); dotted red), upper- and lower-state broadening (first two terms of Equation (9), dotted–dashed turquoise), and all three terms of Equation (9) shown in black; the T-matrices used to produce these calculations include exchange. The ground state contributes significantly to the broadening in the Lyα red wing, and at detunings less than -1 eV, the correlation correction terms contribute extra broadening. There is a singularity at the location of Lyβ, where the profile increases sharply, then, between 1.888 eV $< \Delta\omega <$ 2.8 eV, the profile goes negative, which arises due to the interference between $n = 2$ and $n = 3$ that was discussed in Section 4.1.

paper, the matrix elements are omitted only for D on the left-hand side of $R(\omega)$, which creates the behavior that results in a negative opacity at Lyβ. The full dipole matrix on the RHS of $R(\omega)$ is retained from here on.

4.2. The Quantum-mechanical Broadening due to the 1s State: Nonnegligible Lower-state and Correlation Broadening

The no-lower-state broadening approximations and classical approximations are tied together. Exchange interactions are particularly important to accurately describe the elastic collisions of the $1s$ ground state. Figure 5 demonstrates how the T-matrix solutions are altered when exchange interactions are included compared to when they are omitted. Both calculations predict the presence of H^- resonances, but only the proper inclusion of exchange puts the resonances much closer to the correct energies. Without exchange, the $n = 2$ doubly excited autoionizing state structure looks nothing like detailed calculations or experiments. Here, the widths are far larger than with exchange. Even with exchange, our calculations do not exactly match with other more detailed calculations, such as calculations that use the variational method (A. K. Bhatia et al. 1967; A. K. Bhatia & A. Temkin 1969). We note that, while the bound state and autoionizing state energy levels of H^- calculated using the scattering method have slightly less binding energy than the variational method, the energy level structure closely resembles that of variational method calculations. In Table 1, we compare the locations of various H^- features with quantities from other calculations.

The contribution from the lower-state broadening does not contribute much to the core and is almost entirely canceled out by the correlation term (last term of Equation (5) or third and fourth terms of Equation (9)). In the line wings, the contribution from $1s$ increases significantly. Further, even the correlation term of Equation (9) does not decrease broadening at all frequencies, but increases broadening away from the line center. One interesting and maybe somewhat counterintuitive result is that the correlation term creates more broadening in the line wing rather than less broadening. This effect is attributed to the change in the sign of the real part of the collision amplitudes between the upper and lower states at frequencies away from the line center. Physically, this means that the shifting of the energy levels due to the perturbation is larger than if the energy levels were shifted independently of each other. We demonstrate the impact of the lower-state and correlation terms on the line wings in Figure 6.

4.3. Summary of VCS Approximations

The approximations used by VCS are valid only in the line core. We find that, in the line wings, three out of the four primary approximations, dipole (T. A. Gomez et al. 2024), no-quenching, and classical (the latter two are explored in Section 4.2), by VCS listed above are not valid. Further, these approximations are interconnected. The no-quenching approximation for the upper state is not valid in the wings, where we have demonstrated some interference between the different energy levels. However, if the classical and dipole approximations are removed, the no-quenching approximation for the lower state is no longer valid. In this section, neither the BALROG nor the SIMU calculations employed the dipole approximation, and it will not be used again going forward.

Therefore, we see that, in a quantum treatment of the electron broadening, the lower-state and correlation broadening cannot be ignored. By extension, the additional broadening terms that describe transient stages of the collision, $M_{\mathrm{transient}}(\omega)$, need to be explored in order to have confidence in the calculated wing opacity.

5. Transient Stages of Collisions and the Formation of H^- Features

We reiterate that Equation (9) is not a complete description of the broadening over the entire frequency range. One way in which this is evident is in using a distorted-wave treatment (D. H. Sampson et al. 2009). Rederiving the U. Fano (1963) results with a distorted-wave approach shows that different distortion potentials should result in the same line shape. However, if only the terms in Equation (9) are included, the line

Table 1
Energies of H^- States Calculated Using Scattering Formalism Compared against Literature Values

State	E (This Work)	E (Ref)	
$1s^2\ ^1S$	−0.524	−0.527	H. A. Bethe & E. E. Salpeter (1957)
$2s\ 2p\ ^3P$	−0.142	−0.14259	A. K. Bhatia & A. Temkin (1969)
		−0.142407	A. K. Bhatia et al. (1967)
$2p^2\ ^3P^e$	−0.12525	−0.125355	M. Bylicki & E. Bednarz (2003)

Note. The scattering method is not expected to be as accurate as variational methods used throughout the literature. All energies are in Hartree atomic units.

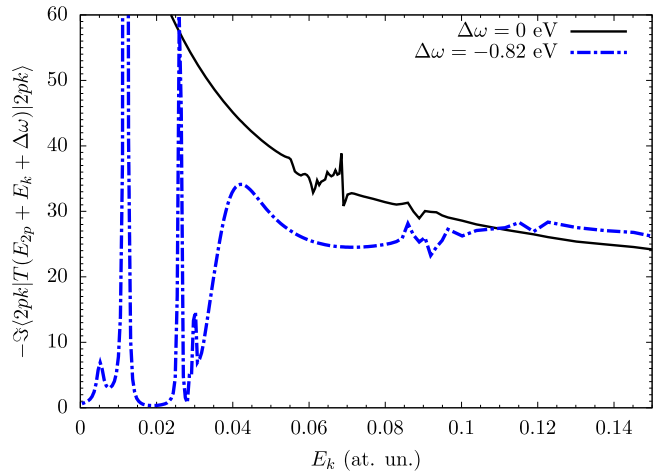

Figure 7. Thermally averaged T-matrix calculation for the $2p$ state at line center (on-shell; black) and at a position off-the-energy shell that corresponds to $\Delta\omega = -0.82$ eV (blue). At the line center, clear doubly excited $n = 3$ and $n = 4$ resonances appear. However, only away from the line center are the (rather large) $n = 2$ resonances present.

shape diverges in the far wings for different distorting potentials, indicating that the formulation is not complete. This result, in addition to the algebraic properties of the formula, indicates that the transient terms of the collisions are needed to have a complete description of the broadening. Indeed, in tests that we have performed with the transient parts of the collision included, the resulting profile is independent of the choice of distortion potential (within some small numerical tolerance). Since the broadening of the $1s$ ground state significantly contributes to the Lyα broadening in the line wings (see Figure 6), the inclusion of the transient terms should be explored.

One of the most significant features that arises in these calculations is the presence of H^- features. In the on-shell calculations (corresponding to the line center), there are clear resonances below the $n = 3$ and $n = 4$ thresholds, but the $n = 2$ resonances, which are below the threshold, are not present. However, the off-shell T-matrix solutions (corresponding to energies away from the line center) contain the $n = 2$ resonances, which are some of the strongest in the spectrum and are now counted as part of the integration when calculating the width; the T-matrices are shown in Figure 7.

There are two types of H^- resonances that appear in the calculation that deserve consideration: stable and autoionizing states. The ground state of H^-, $1s^2\ ^1S_0$, is well known (S. Chandrasekhar 1944) as the only stable state of H^- and has been determined to be an important opacity source in the Sun (I. Hubeny & D. Mihalas 2014). However, there is a second bound state of H^-, as discussed by G. W. Drake (1970) and M. Bylicki & E. Bednarz (2003); this is the doubly excited $2p^2\ ^3P^e$ state, which is stable in nonrelativistic calculations with an energy of $\sim$−0.125355 hartrees. These bound states are captured in the real part of our T-matrix calculations because they are below continuum thresholds. The bound states have no width to them, meaning they will have no corresponding feature in the imaginary part of the T-matrix and are singular. The autoionizing states are energetically above the continuum and manifest as resonances with a finite width (A. R. P. Rau 1996). As a result, the autoionizing states will appear in both the real and imaginary parts of the calculation. As we demonstrate throughout the rest of this section, both of these types of H^- states are observed in the spectrum of Lyα.

The upper-state and lower-state contributions to $\mathcal{H}(\omega)$ will only show autoionizing resonances in the imaginary part (the width), meaning that stable bound states will only contribute to the real part and not to the imaginary part of the upper- and lower-state broadening terms. Because the upper-state broadening terms contain H^- features (e.g., $2p$, nl configurations), it would therefore make sense that the transient terms would also include H^- features, and indeed, they are distinct in the resulting broadening operator. Further, the transient terms result in stable states of H^- contributing to the imaginary part of $\mathcal{H}(\omega)$ and not just the autoionizing ones. Unlike the transient molecular resonances (N. F. Allard et al. 1999), these resonances from H^- result in broad features.

The transient terms can be derived by convolving the frequency evolution of the upper state and lower state. $M_{\rm transient}(\omega)$ is explicitly defined as (U. Fano 1963)

$$M_{\rm transient}(\omega) = \frac{1}{2}\left\{-\frac{T(E_l)T^*(E_l-\omega) - T(E_r)T^*(E_r-\omega)}{E_l - E_r} + \frac{T(E_l^*+\omega)T^*(E_r^*) + T(E_r^*+\omega)T^*(E_r^*)}{E_l^* - E_r^*}\right.$$
$$\left. + \text{p.v.}\frac{T(E_l)T^*(E_l-\omega) + T(E_r^*+\omega)T^*(E_r^*)}{E_l - \omega - E_r^*} - \text{p.v.}\frac{T(E_l^*+\omega)T^*(E_l^*) - T(E_r)T^*(E_r-\omega)}{E_l^* + \omega - E_r}\right\}$$
$$+ \frac{\text{p.v.}}{2\pi i}\int_{-\infty}^{\infty} d\psi\left[\frac{1}{\psi - E_l} - \frac{1}{\psi - \omega - E_l^*}\right] \times \left[\frac{1}{\psi - E_r} - \frac{1}{\psi - \omega - E_r^*}\right] T(\psi)T^*(\psi - \omega), \quad (20)$$

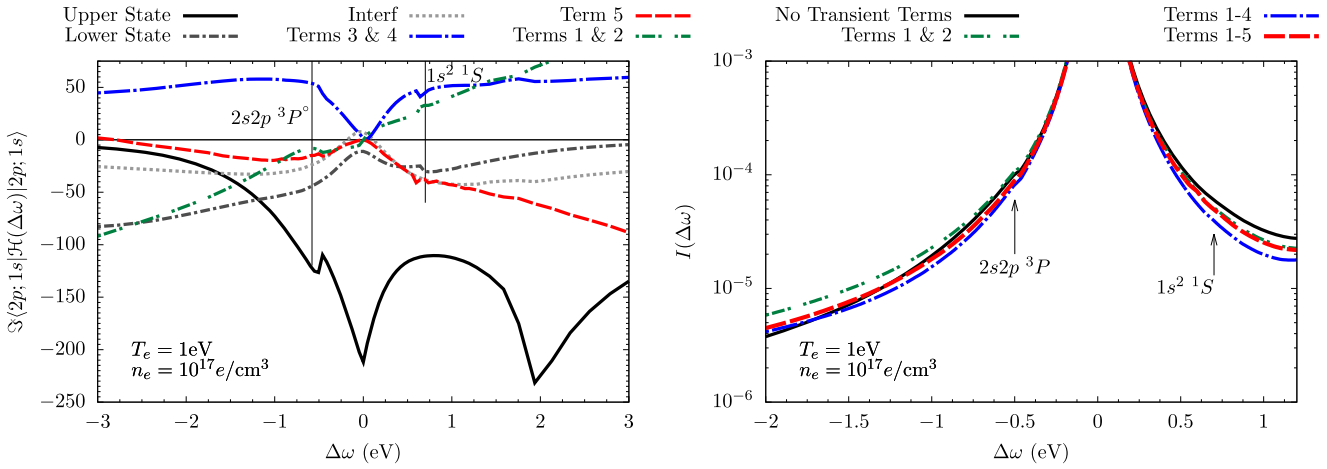

Figure 8. Left: comparison of the different contributions to the broadening operator. The usual terms in Equation (9) are given in solid black, short-dash gray, and dotted light gray. The transient terms from Equation (20) are given in dotted–dashed–dot green (terms 1 and 2), long-dashed–dotted blue (terms 3 and 4), and dashed dark red green (term 5). The calculations presented here only include up to $\mathcal{L} = 4$, where all of the broadening of $1s$ occurs. The basis set here includes only up to $n = 3$. Right: a demonstration of the impact of including various transient terms in the final profile. The solid black line includes no transient terms, the dashed dark red includes terms 1 and 2, the long-dashed–dotted blue line includes terms 1 through 4, and the dotted–dashed–dotted green line includes all transient terms.

where the energy parameters, labeled E, include both radiator and perturber energies, and the subscripts r and l on the energies indicate the state from the right (bra) and left (kets), respectively, of the T-matrices. Here, ψ is an energy, but in this context is treated as a free parameter, rather than (in the usual scattering context) being associated with the energy of the initial or final state of the scattering event. Energies with the * superscript indicate a lower state as well as a complex conjugate. These contributions arise solely from the transient stages of collisions between the radiating atom and the perturbing electrons; a full discussion is given in Appendix B.

The contribution of the individual terms of Equation (20) to the imaginary part of the broadening operator is demonstrated in Figure 8. The usual contributions (Equation (9)) are shown in different shades of gray, while the transient terms (Equation (20)) are in various colors, with the first two terms in dashed dark red, terms 3 and 4 in dotted–dashed blue, and the final term in dotted–dashed–dotted green.

One expected outcome is that all of the transient terms are zero at $\Delta\omega = 0$. As already stated in U. Fano (1963), the line center is the long-time limit and corresponds to completed collisions. Therefore, since the remainder of the terms corresponds to the transient effects, we would expect them to vanish in the limit of long times, which is the line center. Further, if the T-matrices, $T(\psi)$, were independent of ψ, then $M_{\mathrm{transient}}(\omega) = 0$.

Terms 1 and 2 of Equation (20) are asymmetric about the line center, adding broadening on the red side of the profile and reducing the broadening on the blue side of the profile. Terms 3 and 4 of Equation (20) are symmetric around the line center, reducing the broadening on both sides of the profile. The final term of Equation (20) adds a bit of broadening back in, canceling some, but not all, of terms 3 and 4, and has a slight asymmetry that counters terms 1 and 2.

Figure 8 demonstrates various H^- features in the broadening operator and the associated changes in the line shape. It is clear that, without the transient terms, the $2s\,2p\ ^3P$ autoionizing resonance is present in the line wing about 0.5 eV from the line center on the red side of the profile. When the transient terms are included, the stable $1s^2\ ^1S$ state appears on the blue side of the wing.

6. Comparison of Calculations

We would like to spend some time identifying the cause for different broadening effects. Already in Figure 3, we showed that BALROG, VCS, and SIMU give the same line shape (except for BALROG due to detailed balance affecting the red wing of the profile) when each calculation makes the same approximations. As a reminder, these approximations include no-quenching and dipole approximation.

We repeat the comparison of BALROG against VCS in Figure 9, where BALROG now uses a full-Coulomb interaction, includes exchange, no longer makes the no-quenching approximation, and includes the transient terms. The removal of the no-quenching approximation is needed in order to capture the H^- autoionizing states, which adds to the structure of the wings. BALROG now shows a slight enhancement in the blue wing of the profile compared to VCS. Further, the structure of the $1s^2\ ^1S$ ground state is present, as indicated above. The red wing has now been increased and agrees well with VCS except in the location where the H^- resonance is at ∼0.55 eV.

Next, we want to discuss the impact of increasing the basis set size on the profiles. The differences between BALROG and VCS when the former uses the $n = 2$ basis result in fairly similar profiles. However, when $n = 3$ is included, the opacity in the wings is raised above that of VCS. This behavior is expected as increased basis sets tend to increase the broadening. SIMU calculations confirm that including $n = 3$ raises the opacity. The SIMU and BALROG calculations are fairly close in the red wings except around the H^- autoionizing feature, of course.

Lastly, when including $n = 4$ into the calculation, the opacity in the wings increases even further over the $n = 3$ calculations. The increase in the opacity going from $n = 3$ to $n = 4$ is less than that from $n = 2$ to $n = 3$, so there is some confidence that we are approaching convergence for the calculation. We acknowledge that, while we are approaching convergence, these calculations are not converged, and there will be some uncertainty from neglecting states higher than $n = 4$, including

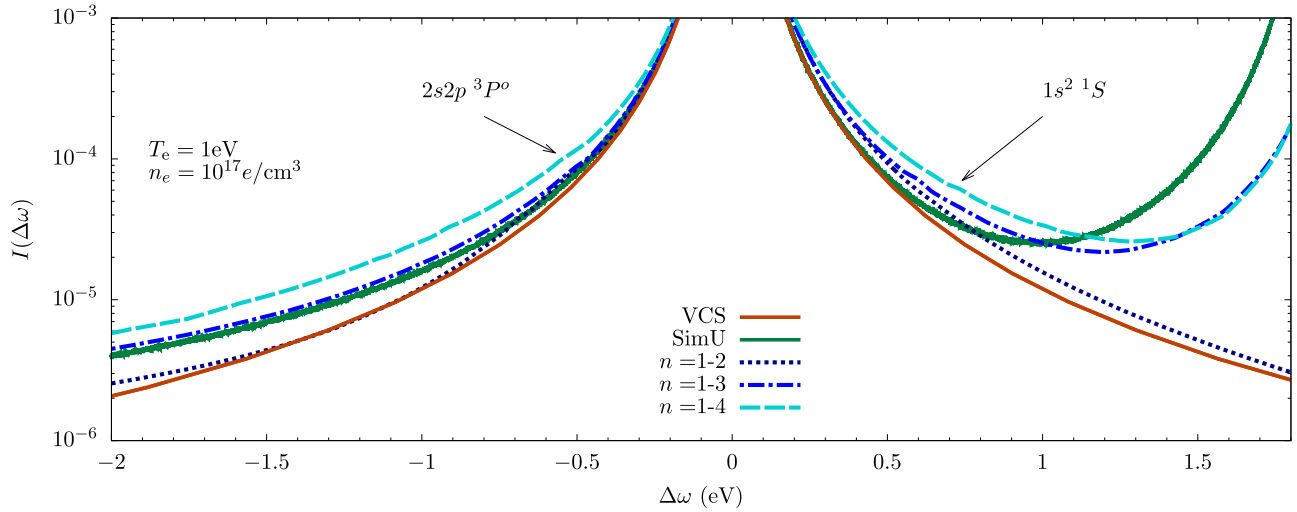

Figure 9. Comparison of the new BALROG calculations (various shades of blue) against VCS (dark orange) and SIMU (dark green). The SIMU calculations presented here include up to $n = 3$ and use a full-Coulomb interaction. BALROG calculations were performed with a variety of different basis sets; this is done to isolate the effect of including a larger basis set. For instance, when only $n = 1$ and 2 were included, the red wing followed VCS quite closely except for the presence of the autoionizing feature at ∼0.55 eV. Increasing the number of states in the calculation increases the opacity; this is seen not only in the various BALROG calculations but also in SIMU. The BALROG calculations that include $n = 4$ have 90% and 180% increased opacity over VCS at $\Delta\omega = -0.55$ and -2 eV, respectively. We point out that even the BALROG calculations are not converged here, and the inclusion of a larger basis is prohibitively expensive to calculate.

continuum states. Including even $n = 5$ is computationally prohibitively expensive due to the additional amount of data that is needed to calculate the line shape. One of the *major* memory sinks in the calculation is storing the fully off-shell T-matrices before performing the integration over the projectile electron's energy.

It is clear that the new quantum-mechanical calculations are the broadest of all of the presented calculations here. The increase in the red-wing opacity is not a small correction but rather is a quite significant change compared to VCS. Much of this behavior is due to the broad H^- features that now appear in the calculation, as well as the larger basis set in which the calculations are performed. The opacity of the Lyα red wing at $\Delta\omega = -0.5$ eV and $\Delta\omega = -2$ eV has increased by 90% and 180%, respectively, over VCS when the $n = 4$ states are included in the calculation. It is also clear from this comparison that the new calculation has a flatter slope compared to VCS, meaning that the decay of the profile is not as fast as previously predicted, and the opacity discrepancy will get worse as the detuning becomes large. The SIMU calculation presented here is instructive because it also shows a different slope than what is predicted by VCS despite also being a classical calculation.

7. White Dwarf Atmospheres

In the analysis performed above, it is clear that there are some effects from treating the broadening quantum-mechanically. Of the calculations we compare here, only BALROG (T. A. Gomez et al. 2021) contains the quantum behavior of the plasma electrons. Therefore, in our comparison of WD spectra, we compare only BALROG and VCS/Tremblay–Bergeron calculations. We note that the P. E. Tremblay & P. Bergeron (2009) Lyα calculations are identical with VCS. To generate model atmospheres and synthetic spectra, we use the program TLUSTY (I. Hubeny & T. Lanz 1995; I. Hubeny et al. 2021), appropriately modified to incorporate new line-broadening data. We note that, in a few of our comparisons, the $T_{\rm eff}$ of the WD models is below 15,000 K. At these temperatures, the atmosphere model must include a treatment of convection (P. Bergeron et al. 1995), whether it is through mixing length theory or 3D hydrodynamical calculations (P. E. Tremblay et al. 2011).

As mentioned above, modeling H_2^+ features in WD spectra are necessary. The N. F. Allard et al. (1999) models that are used for this purpose are ion-only profiles. We stress that the original Allard/Koester calculations have been improved (D. Koester 2024, private communication), and the corresponding line-broadening tables are now implemented in TLUSTY. These tables separately describe broadening by hydrogen atoms and protons, while broadening by electrons is described by a semiclassical formula. Therefore, in the atmosphere models, one would have to convolve (if one cannot solve both of them together) an electron-only profile with an ion-only profile. Because VCS calculations of electron-only broadening are not available, atmosphere codes use one-half of the intensity of the VCS ion+electron profile calculations to approximate the electron profile. Instead of performing a true convolution, it is approximated in the atmosphere models by adding one-half of the VCS profile to the Allard H_2^+ to make the final profile. This procedure has the issue of doubling the strength of Lyα in the core of the profile. At lower temperatures, this doubling is not an issue, but at hotter temperatures, where the Lyα line is not as saturated, this might pose a problem for obtaining accurate opacities. The profiles that we provide here are electron-only profiles and can be used in place of the one-half VCS profile. When using recent calculations by Koester, we replace his semiclassical treatment of electron broadening with our present calculations, while keeping the calculated tables of broadening by H_2^+ and H_2. This grid of new profiles will be made available on the TLUSTY website.[11]

One of the immediate results of this work is that, for low-temperature WDs, the increased opacity from the $2s\,2p\ ^3P^o$ resonance is observable in the emergent spectra. Figure 10 demonstrates quite clearly a change in the slope of the Lyα red

[11] https://www.as.arizona.edu/~hubeny/tlusty208-package/

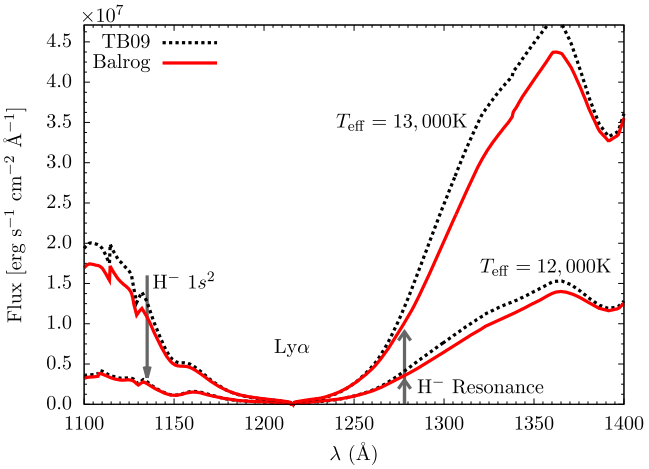

Figure 10. Comparison of BALROG and Koester profiles in an atmosphere, calculated with TLUSTY. The atmosphere calculations of TLUSTY with BALROG profiles predict that the H^- resonances will be present and even measurable in cool WDs in the UV; $\log g$ is assumed to be 8 for all spectra. Likewise, there is a change on the blue side of the profile corresponding to the increase in opacity from the ground state of H^-.

wing that begins exactly where the resonance occurs. Redward of the H^- resonance at 1278 Å, there is less flux in the new model. Additionally, there is another change in the slope of Lyα where the ground state of H^- occurs, which is indicated by a lower flux blueward of 1135 Å. Unfortunately, these features are not observable with HST's COS as the 1278 Å resonance is in the gap between the two chips on the spectrometer, and the H^- ground state feature is at the blue edge of the spectrometer, making observations of these changes difficult. The future NASA mission ARCUS will have the UV capability to be able to measure these differences predicted by these models.

It is clear that, with the extra opacity in the line wings, the absorption due to Lyα is stronger. This trend is in the correct direction for the analysis of cool WDs. For example, in S. Sahu et al. (2023), the spectral fits of Lyα were cooler than determined from the Balmer lines. With the present extra Lyα broadening, the temperature would have to be increased in order to match the data, thus decreasing (if not eliminating) the current temperature discrepancy to the Balmer lines.

The primary results regarding flux distribution are shown in Figure 11. The differences between the calculations are apparent between 20,000 and 12,000 K, where most of the flux of WDs is in the same region as the Lyα line. Figure 11 also shows the visible-light spectrum, focusing on the high-n Balmer lines. The increased opacity has redistributed some of the flux from the UV into the visible, and now, the visible is slightly brighter by up to a few percent. While this may not seem to be a large increase, it is larger than the estimated errors ($\lesssim$0.5%; R. C. Bohlin et al. 2020) on the HST spectra calibration that come from atmosphere models like TLUSTY. Since atmosphere models are used in the calibration of HST spectra, then the change in the visible flux will modify the HST calibrations for all other spectra taken with that instrument.

Additionally, we compared the normalized line shapes of the Balmer series with the new Lyα profiles. Surprisingly, the normalized line shapes were largely unchanged by the new Lyα profiles. We therefore expect that, as far as obtaining $\log g$ from the Balmer series, this work will not significantly affect the determinations of gravity. We do expect that the determination of temperature and gravity from the Lyman series will be affected.

Since the overall flux in the visible is changed, that means that estimates of WD parameters like radius and temperature will change. Telescopes like Gaia can measure distances directly, so atmosphere models can be used to infer stellar radii and luminosities from the observed photometric intensity, in addition to the effective temperature and surface gravity. Changes to the total modeled flux in the visible, where many WD stars are observed, can therefore modify many different stellar parameters. For example, if the estimated luminosity of a star is changed, because of the increase in modeled visible flux, then the inferred radius or temperature of the star must also change. A preliminary analysis has shown that the increase in the modeled flux in the visible will translate to a change in the effective temperatures in some stars of up to a few hundred degrees.

Lastly, we want to make a quick note on the dependence with gravity. For atmosphere models in Figures 10 and 11, we only showed a "typical" WD gravity, of $\log g = 8$. As the gravity of the star increases, the density at the photosphere becomes larger. Therefore, the changes in the model are likely to be stronger, and we would expect changes in the visible spectrum to be greater for stars with larger gravity. Conversely, stars with lower gravity will likely not show as large of a difference in the visible.

A detailed analysis of how much WD temperature, gravity, or radius determinations change due to the new Lyα profile is beyond the scope of the current work.

8. Future Work

Unfortunately, the work provided here is not the final word regarding the most physical Lyα profiles. We have so far neglected to include the correlations in the density matrix. This correction to the density matrix has been shown to result in an asymmetry of the profile (T. A. Gomez et al. 2018). M. Baranger (1958a), as well as U. Fano (1963), has stated that the inclusion of the correlations in the density matrix will not affect the line core, and that is why it will often be ignored. When the detuning, $\Delta\omega$, is of the order of the temperature, T, this effect will become significant.

Lastly, there are some trivial frequency dependencies that are associated with the radiation process that still need to be included. Trivial frequency dependencies are factors of the frequency that are intrinsic to the interaction of radiation with the atom, rather than belonging to the frequency-dependent broadening caused by the plasma. By this, we mean factors of ω that indicate absorption and factors of ω^4 for the radiated power (H. R. Griem 1974). These trivial frequency dependencies are often neglected when the focus is on the small range of ω around the line center. In the case that we are exploring here, we are concerned with detunings $\sim$2 eV from a line at 10.2 eV, meaning that $\Delta\omega/\omega_{\rm Ly\alpha}$ is of order 20%, which cannot be neglected.

Additionally, the impact of plasma oscillations has been neglected here. It is not expected to contribute significantly to the line shape (H. R. Griem 1974). Plasma oscillations create satellites at detunings with integers of the plasma frequency (I. Hannachi et al. 2023), whose intensity depends on the level of excitations of these oscillations.

We point out that there are other broadening sources beyond what have been explored here. For instance, neutral broadening

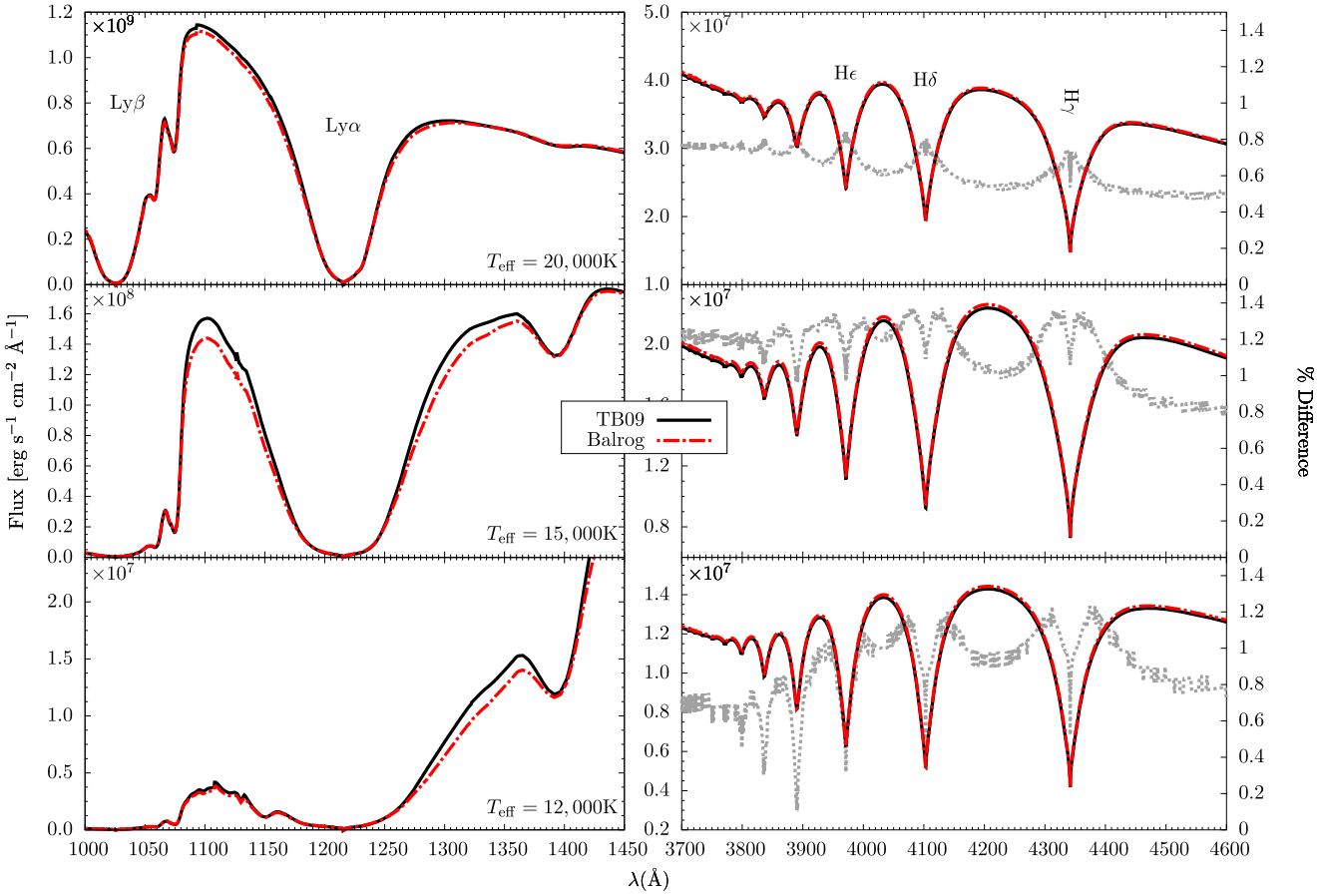

Figure 11. Comparison of BALROG (dotted–dashed red) and Koester profiles (solid black) in an atmosphere, calculated with TLUSTY. All gravities are set to $\log g = 8$. The additional broadening in Lyα is apparent. Another consequence of the increased opacity is the rising of the flux in the visible part of the spectrum. Also plotted is the percent difference in visible flux in dark gray.

has been calculated by N. F. Allard et al. (2000). However, it is important to point out that a self-consistent calculation that includes electron broadening, H^+, and H satellites does not exist. Additionally, accounting for accurate collisions involving three particles has not been included in any calculations. Simulations can include multiple simultaneous collisions, but, as pointed out in T. A. Gomez et al. (2024), the satellite features of even binary collisions are formed at the incorrect energy.

9. Summary and Conclusions

Broad and saturated spectral lines are an important source of opacity in hot stars. Therefore, the structure of WD atmospheres is sensitive to the broadening of Lyα, so much so that changes in the wing opacity, which is 10^5–10^6 orders of magnitude less intense than the core of the line, can affect the flux distribution of the stellar spectrum even into the visible region.

In the wings, there are resonant H_2^+ features easily observed in WD spectra. As in the ion cases, the electrons in the atmosphere will make transient H^- during their collisions with the radiators. The industry standard electron-broadening model, VCS, does not include this effect. In this work, we explored the effect of H^- on the spectral line shapes and WD atmospheres.

We compared different calculations of electron broadening of Lyα at conditions relevant to WD photospheres. We point out that VCS makes a number of simplifying approximations that are not applicable to the far wings of the line, which dictate the opacity in WDs. Under similar approximations, we find that the VCS calculations agree quite well with other calculations, such as SIMU and BALROG.

The inclusion of H^- in BALROG caused distinct features to appear in the spectra. Specifically, there was an enhancement of the opacity starting around −0.55 eV and continuing to the red part of the profile. This enhancement corresponds to the H^- autoionizing state, $2s\,2p\ ^3P$. Additionally, there is also a slight change in the wing behavior due to the $1s^2\ ^1S$ ground state, which, instead of a broad enhancement, produces more of a localized feature.

Additionally, the VCS calculations use a limited basis set when performing their calculations. Neither SIMU or BALROG are bound by this limitation, and we can increase the number of atomic states considered for the calculation. Adding more states usually results in asymmetries and additional redshifts. We, therefore, see increases in the red-wing opacity in both SIMU and BALROG. When including up to $n = 4$, combined with the H^- features, BALROG predicts 90% to 180% increases in opacity over VCS between $-2 < \Delta\omega < -0.5$ eV—a significant enhancement.

When using the BALROG profiles in a WD atmosphere, it has a severe effect on the Lyα spectrum between 20,000 and 12,000 K. The broader profiles substantially increase the opacity compared to the VCS model. This increased opacity changes the emergent spectra of the Lyα line. Further, the additional opacity from the extra broadening causes increases

in the visible flux. This result will affect HST spectrometer calibrations and modify the emergent model spectral lines used to determine the gravity and mass of WDs.

Some of the prominent changes in the line shape are not observable with the current UV instruments on HST. We anticipate that the future NASA mission, ARCUS (which is currently planned to have a UV spectrometer), should be able to measure the changes we predict in the spectra with ease.

Lastly, we make these profiles available to the WD community, available to download on the TLUSTY website.[12]

Acknowledgments

We thank Prof. K. France for useful references. T.A.G. acknowledges support from the George Ellery Hale Postdoctoral Fellowship at the University of Colorado. M.H.M. and D. E.W. acknowledge support from the United States Department of Energy under grant DR-SC0010623 and the Wootton Center for Astrophysical Plasma Properties under the United States Department of Energy collaborative agreement DE-NA0004149. J.R.W. acknowledges support from the U.S. DOE NNSA SSGF program under DE-NA0003960. J.R.W., M.C.Z., and C.J.F. acknowledge support from the Los Alamos National Laboratory (LANL) ASC PEM Atomic Physics Project. LANL is operated by Triad National Security, LLC, for the National Nuclear Security Administration of the U.S. Department of Energy under contract No. 89233218NCA000001. I.B. acknowledges the Australian Research Council and the support of the National Computer Infrastructure and the Pawsey Supercomputer Centre. The work of E.S. was partly supported by Sandia National Laboratories (USA) and by the University-of-Michigan Multi-University Center of Excellence for Magnetic Acceleration, Compression, and Heating (MACH).

Appendix A
Calculation of *T*-matrices

The collision T-matrix is closely related to the collision amplitude (M. Baranger 1958a). The T-matrix also obeys the optical theorem, where the imaginary part is related to the total collision cross section; see Section 2 in the main text. The T-matrices are defined in terms of the interaction potential V, the noninteracting Hamiltonian terms, H_0, and an energy parameter, ψ. We point out that ψ has a small implied imaginary part, and it is understood that we take the limit that the imaginary part goes to zero. To obtain the desired electron-broadening operator, we need to consider off-the-energy-shell T-matrices. Off-the-energy-shell matrix elements are those where ψ does not equal the energy of either state of the matrix element, i.e., if we have the matrix element, $\langle\alpha|T(\psi)|\beta\rangle$, then

$$\begin{cases} \psi = E_\alpha = E_\beta & \text{on-shell} \\ \psi = E_\alpha \neq E_\beta & \text{half-on-shell} \\ \psi = E_\beta \neq E_\alpha & \text{half-on-shell} \\ \psi \neq E_\alpha \quad \text{and} \quad \psi \neq E_\beta & \text{fully-off-shell} \end{cases}. \tag{A1}$$

Since the calculations presented here rely on the fully off-shell T-matrices, we need to modify how we obtain our solution compared with previous methods; we outline this change here. We emphasize here that the T-matrices are all-order calculations, meaning that we are solving

$$T(\psi) = \frac{1}{1 - V(\psi - H_0)^{-1}} V \tag{A2}$$

exactly, using a linear solver (i.e., $Ax = b$) routine,

$$[1 - V(\psi - H_0)^{-1}]T(\psi) = V, \tag{A3}$$

where

$$A = [1 - V(\psi - H_0)^{-1}],\ x = T(\psi),\ \text{and}\ b = V. \tag{A4}$$

When exchange is included, the V operator includes a space-exchange operator as well as a term that depends on the parameter ψ,

$$V_{ap} = \frac{1}{|\boldsymbol{r}_a - \boldsymbol{r}_p|} - \frac{1}{|\boldsymbol{r}_p|} + (-1)^S[H - \psi]P_r. \tag{A5}$$

These calculations are made simple because the V-matrix (and by extension the T-matrix) is diagonal in the total spin, S, as well as the total angular momentum, L.

A.1. Important T-matrix Relationships

An important quantity related to the T-matrix is the so-called K-matrix or reactance matrix. The K-matrix is defined as

$$K(\psi) = \frac{1}{1 - V\frac{\text{p.v.}}{\psi - H_0}} V, \tag{A6}$$

and is Hermitian. The T-matrix can be defined in terms of K-matrices:

$$T(\psi) = \frac{1}{1 + i\pi K(\psi)\delta(\psi - H_0)} K(\psi). \tag{A7}$$

The K-matrix is obtained by separating out the real and imaginary parts of the Green's function. Here, we use the definition

$$\frac{1}{\psi - H_0} = \lim_{\eta \to 0} \frac{1}{\psi + i\eta - H_0} = \frac{\text{p.v.}}{\psi - H_0} - i\pi\delta(\psi - H_0). \tag{A8}$$

The K-matrix can be used to rigorously derive the optical theorem,

$$T(\psi) = K(\psi)\frac{1 - i\pi\delta(\psi - H_0)K(\psi)}{1 - i\pi\delta(\psi - H_0)K(\psi)}\frac{1}{1 + i\pi\delta(\psi - H_0)K(\psi)}, \tag{A9}$$

then separating the individual contributions,

$$T(\psi) = K(\psi)\frac{1}{1 + [\pi\delta(\psi - H_0)K(\psi)]^2} - i\pi K(\psi)\frac{\delta(\psi - H_0)K(\psi)}{1 - i\pi\delta(\psi - H_0)K(\psi)}\frac{1}{1 + i\pi\delta(\psi - H_0)K(\psi)}, \tag{A10}$$

[12] https://www.as.arizona.edu/~hubeny/tlusty208-package/

the imaginary part of the T-matrix is defined in terms of a product of T-matrices:

$$\begin{aligned}\Im T(\psi) &= -\pi K(\psi)\frac{1}{1 - i\pi\delta(\psi - H_0)K(\psi)} \\ &\quad \times \delta(\psi - H_0)K(\psi)\frac{1}{1 + i\pi\delta(\psi - H_0)K(\psi)} \\ &= \pi T^{\dagger}(\psi)\delta(\psi - H_0)T(\psi). \end{aligned} \tag{A11}$$

Due to the relationship between the T-matrix and the collision amplitude (M. Baranger 1958a; I. Bray & A. T. Stelbovics 1992), it is clear how the width (which comes from the imaginary part of the collision amplitude) can be equated to a sum of cross sections.

There is another important consequence of the optical theorem in Equation (A11) having to do with unitarity. The T-matrices are closely related to the scattering S-matrix,

$$S = 1 + 2i\pi\delta(\psi - H_0)T(\psi), \tag{A12}$$

and the S-matrices are unitary,

$$SS^{\dagger} = I. \tag{A13}$$

The optical theorem can be derived from the unitary relationship here, meaning that satisfying the optical theorem is a direct consequence of obeying unitarity. The unitarity property is important in our calculations as it ensures that the total probability equals 1. There is also a further statement, not considered here, about the unitary property being important for particle conservation. In T. A. Gomez et al. (2021), the supplementary material demonstrated that Equation (A11) is satisfied to machine precision using the method of the solution described here.

A.2. Calculation of Screened Coulomb Potentials

In the screened Coulomb problem, one can use a partial wave expansion to define the Coulomb problem in terms of spherical harmonics (M. C. Zammit et al. 2010),

$$\frac{e^{-\kappa|r_1 - r_2|}}{|r_1 - r_2|} = -4\pi\kappa\sum_{t=0}^{\infty} j_t(i\kappa r_<)h_t^{(1)}(i\kappa r_>)\sum_q Y_{tq}^*(\hat{r}_1)Y_{tq}(\hat{r}_2), \tag{A14}$$

which reduces to the usual expression for the Coulomb interaction,

$$\lim_{\kappa\to 0}\frac{e^{-\kappa|r_1 - r_2|}}{|r_1 - r_2|} = \sum_t \frac{r_<^t}{r_>^{t+1}}\frac{4\pi}{2t+1}\sum_q Y_{tq}^*(\hat{r}_1)Y_{tq}(\hat{r}_2). \tag{A15}$$

However, rather than performing 2D integrals, the Balrog code instead solves the screened Poisson equation. Given a density distribution, $\rho(r)$, the screened Poisson equation is

$$[\nabla^2 - \kappa^2]V(r) = -4\pi\rho(r). \tag{A16}$$

In an atomic physics problem, $\rho(r)$ is a product of wave functions. Using the expansion in Equation (A14), we can write the potential from that density distribution as

$$V(r) = \sum_{tq} V^{(t)}(r)\sqrt{\frac{4\pi}{2t+1}}Y_{tq}(\hat{r}). \tag{A17}$$

Because the spherical harmonic is an eigenfunction of the Laplace operator, its associated eigenvalue can then replace the angular part. Lastly, multiplication from the left by $Y_{tq}^*(\hat{r})$, and then factoring out the angular coefficients gives the resulting simplified expression for the radial potential,

$$\begin{aligned}&\left[\frac{d^2}{dr^2} + \frac{t(t+1)}{r^2} - \kappa^2\right][rV^{(t)}(r)] \\ &\quad = -(2t+1)rR_a(r)R_{a'}(r), \end{aligned} \tag{A18}$$

which substantially speeds up calculations, and Equation (A14) is used only to impose boundary conditions. To calculate $rV^{(t)}(r)$, we use an $Ax = b$ solver, where the A matrix is the quantity in big brackets of Equation (A18). The differential operator is replaced by finite difference matrix elements,

$$\frac{d^2}{dr^2} \Rightarrow \frac{1}{(\Delta r)^2}\begin{bmatrix} -2 & 1 & 0 & 0 & \cdots & & & \\ 1 & -2 & 1 & 0 & \cdots & & & \\ 0 & 1 & -2 & 1 & \cdots & & & \\ \vdots & \vdots & \vdots & \vdots & \ddots & & & \\ & & & & & 1 & -2 & 1 \\ & & & & & 0 & 0 & (\Delta r)^2 \end{bmatrix}, \tag{A19}$$

and the other A terms, i.e., $\frac{t(t+1)}{r^2} - \kappa^2$ are included on the diagonal of the matrix. If the b matrix, i.e., $-(2t+1)rR_a(r)R_{a'}(r)$, is left exactly as that and the last element is left as zero, then the solution at the $r = r_0$ boundary will be forced to zero. Therefore, to accurately calculate the large r limit of the potential, the exact solution must be included. This is done by performing the integral of Equation (A14) for the last point on the spatial grid. The $A_{n,n}$ matrix element is set to unity in Equation (A19) to enforce this boundary condition. We note that forcing the solution to zero at the origin is the appropriate boundary condition; hence, the correct solution is generated naturally at $r = 0$.

A.3. Uniqueness in the T-matrix Solution When Exchange Interactions Are Included

It is well known that Equation (A5), is stable for on-shell calculations, but is unconstrained in the off-shell. A. T. Stelbovics & B. H. Bransden (1989) and A. T. Stelbovics (1990) proposed the inclusion of additional boundary conditions to obtain unique solutions regardless of the parameter ψ. I. Bray & A. T. Stelbovics (1992) used the property

$$\langle i_n|f_{mk}\rangle = (-1)^S\langle i_m|f_{nk}\rangle, \tag{A20}$$

where i is an atomic/target state, S is the total spin of the target +projectile system, and f_{nk} is the scattered wave,

$$|f_{nk}\rangle = |\phi_k\rangle\delta_{nk} + \sum\!\!\!\!\!\!\int_n \frac{|\phi_n\rangle\langle\phi_n i_n|V|\phi_k i_k\rangle}{\psi - E_{\phi_n} - E_{i_n} + i\eta}, \tag{A21}$$

to obtain a new effective interaction potential that has unique solutions on the off-shell,

$$\begin{aligned}V_{ap} &= \tfrac{1}{|r_a - r_p|} - \tfrac{1}{|r_p|} \\ &\quad + (-1)^S[H - (1-\theta)\psi]P_r - \theta\psi I_p, \end{aligned} \tag{A22}$$

where

$$I_p = \sum_n |i_n\rangle \langle i_n|, \tag{A23}$$

and θ is an arbitrary nonzero constant. This form is extremely convenient for on-shell calculations, and the T-matrix solution is independent of the choice of θ for on-shell and near-on-shell values.

However, this form creates nonunique solutions for off-shell matrix elements when $\psi = 0$. Since our calculations required stable off-shell T-matrix elements, we tried alternate forms of the interaction potential with the nonuniqueness fix. One choice was to make θ independent of ψ,

$$V_{ap} = \frac{1}{|\boldsymbol{r}_a - \boldsymbol{r}_p|} - \frac{1}{|\boldsymbol{r}_p|} + (-1)^S[H - \psi]P_r + (-1)^S\theta P_r - \theta I_p, \tag{A24}$$

which would fix the nonunique issues at $\psi = 0$. This form has its own downside with the principal one being the analytic behavior of the T-matrix at large ψ. In the limit that $|\psi|$ becomes large, the T-matrix should (when exchange is included) be linear in ψ,

$$\lim_{\psi \to \pm\infty} T(\psi) \propto \psi. \tag{A25}$$

This behavior could not be achieved unless θ was extremely large. Further, when evaluating $M_{\text{transient}}(\omega)$ (Equation (20)), the fifth term became numerically unstable and was not independent of the choice of θ.

Each form for the effective interaction potential has its own advantages and disadvantages. The original form of Equation (A22) is able to produce the expected linear behavior in Equation (A25) much better and at far lower values of θ, but had the problem of having nonunique solutions at $\psi = 0$. Equation (A24) fixed the nonuniqueness issue at $\psi = 0$, but had numerical difficulties when $|\psi|$ became large. For our final form, the interaction potential that we use is

$$V_{ap} = \frac{1}{|\boldsymbol{r}_a - \boldsymbol{r}_p|} - \frac{1}{|\boldsymbol{r}_p|} + (-1)^S[H - \psi]P_r + [|\psi| + \psi_0]\theta((-1)^S P_r - I_p), \tag{A26}$$

where ψ_0 is some offset that prevents the entire quantity in brackets from going to zero. The way we have defined it, ψ_0 has to be positive, although this is not a requirement as long as the entire quantity $[|\psi| + \psi_0]$ is the same sign for all ψ. If one is concerned with only on-the-energy-shell points, ψ_0 could be as small as 0.01 and be sufficient. However, since we are dealing with off-the-energy shell, we chose a larger value of 100 to ensure convergence.

The mathematical form of Equation (A26), unlike the previous forms discussed, has led to invariance of the electron broadening as a function of θ for all terms. The other forms lead to invariance in the usual broadening terms, such as those covered in Equation (9), plus terms 3 and 4 of Equation (B1). But those forms did not lead to unique solutions of terms 1, 2, and 5 of Equation (B1) that were independent of θ. The new form of Equation (A26) preserves invariance in all transient terms.

A.4. The Real Part of the Green's Function

In Balrog's default mode when it performs the integral over the electron momentum, k, to find the T-matrix, it assumes that the potential is constant over some small Δk and then solves the Green's function analytically. The integral is evaluated in terms of a quadrature where the weights are given by

$$w(k_i) = k_i^2 \int_{(k_i + k_{i-1})/2.}^{(k_i + k_{i+1})/2} dk \frac{\text{p.v.}}{\frac{1}{2m}(q^2 - k^2)}, \tag{A27}$$

where $w(k_i)$ is quadrature weights whose solution in this case is

$$w(k_i) = \frac{k_i^2}{|q|} \begin{cases} \ln\dfrac{q-b}{q+b} - \ln\dfrac{q-a}{q+a} & \text{if } q > b \\ \ln\dfrac{b-q}{q+b} - \ln\dfrac{a-q}{q+b} & \text{if } q < a \\ \ln\dfrac{b-q}{q+b} - \ln\dfrac{q-a}{q+b} & \text{if } a < q < b \\ q\left[\dfrac{2}{b} - \dfrac{2}{a}\right] & \text{if } q = 0 \\ 2[\arctan(a/|q|) - \arctan(b/|q|)] & \text{if } q^2 < 0. \end{cases} \tag{A28}$$

Here, a is the lower bound of the integration, $a = (k_i + k_{i+1})/2$, and b is the upper bound of the integration, $b = (k_i + k_{i-1})/2$. This expression works well except at low k where there are issues with convergence. To achieve convergence, integration to extremely high k is necessary, with E_k exceeding 100 hartree.

In this work, we also explored the use of the position representation of the Green's function (A. W. Bray et al. 2015, 2016, 2017), which amounted to the same answers as using the momentum representation described above. We point out that the position Green's function routine that we use here is distinct from that of A. W. Bray et al. (2015, 2016, 2017), where, instead of using a box basis, we take advantage of some analytical properties of the Green's function at large r.

A.5. Convergence of the T-matrix Solutions and Line-shape Calculations

One of the central computational challenges associated with this work is dealing with convergence of the close-coupling equations with an increasing basis size. We want to be clear that this is a separate issue from the stability of the solutions, which was fixed by using the condition from Equation (A20). Convergence of on-shell T-matrices has already been established and is expected; however, this only guarantees stability at the line center. However, as I. Bray & A. T. Stelbovics (1995) demonstrated in Section 5 and Figure 3 of their paper, fully off-shell or half-off-shell calculations do not converge with an increasing basis size. This is a problem because our calculations of the transient parts of the collisions require fully off-shell T-matrix solutions. I. Bray & A. T. Stelbovics (1995) attributed this nonconvergent behavior to the energy terms contained in Equation (A26). Our calculations, which solve for the T-matrices exactly, suffer from this same problem. This lack of convergence is demonstrated in Figure 12 for a K-matrix calculation (upon which the T-matrix is built), where convergence is achieved for the on-shell point, but not anywhere else. We note that changing the value of θ did not alter these results whatsoever.

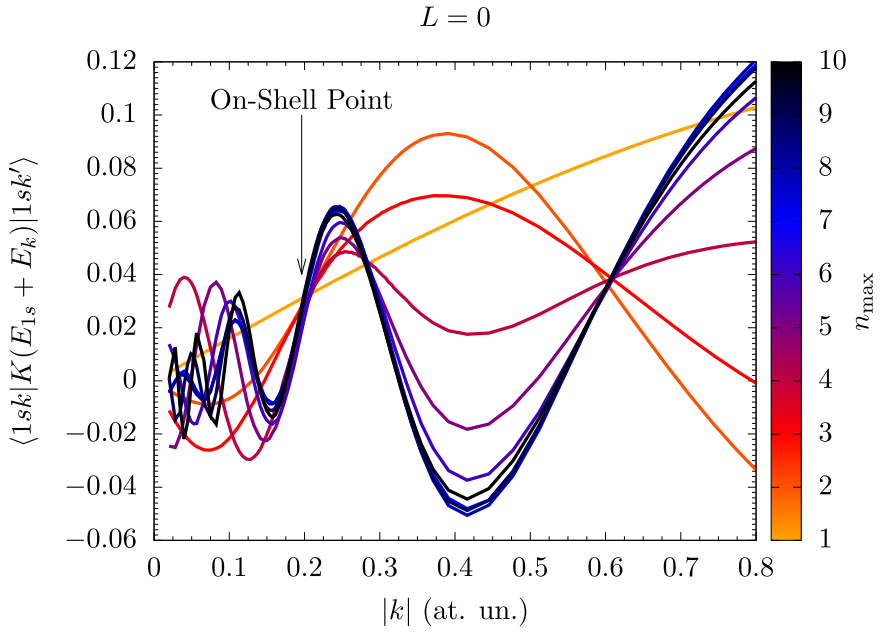

Figure 12. Half-on-shell K-matrix for the $L = 0$ partial wave to demonstrate the convergence of the solution as a function of adding states up to a maximum principal quantum number, $n_{\max}$. The incident k is roughly 0.2 in atomic units.

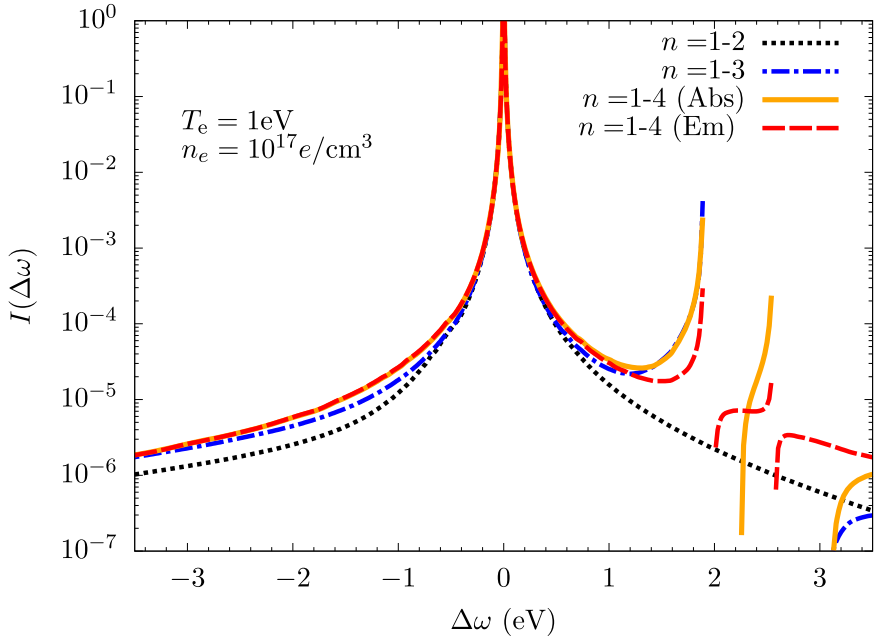

Figure 13. Convergence of the Lyα spectrum with increasing n. The dotted black line only includes $n = 1$ and 2, the dotted–dashed blue line adds $n = 3$, and the orange and red lines are $n = 4$ but with different populations (absorption/emission). Wild oscillatory behavior seen in Figure 12 does not translate to the line profile. There are singularities in the blue wing of Lyα that correspond to interference between different levels. These features will ultimately translate to asymmetries in the Lyβ and Lyγ lines. The shapes of the line transition interference vary with the intensity of the neighboring lines compared to Lyα, and therefore have a different shape in emission vs. absorption.

We performed a number of tests with only s states and found that convergence with basis size could be achieved with direct-only terms of the V-matrix or when monopole exchange terms are not included. In other words, when the total angular momentum, L, equals 1, meaning the projectile angular momentum, l_p, is equal to 1, the resulting K-matrix solutions were stable. When $L = 0$, forcing $l_p = 0$, none of the exchange terms in V resulted in stable K-matrices. This includes the energy terms as well as the electron–electron term.

From Figure 12, it is clear that most of the nonconvergent behavior occurs at low values of momentum, k. At higher values of momentum (and especially near the on-shell point), the K-matrix solution is more stable, appearing to come to some convergence point. This instability of the low-energy points is particularly prominent for the T-matrix elements involving the $1s$ state. The calculation is sensitive to the number of high k points included in the basis set even for on-shell points of $1s$ in particular.

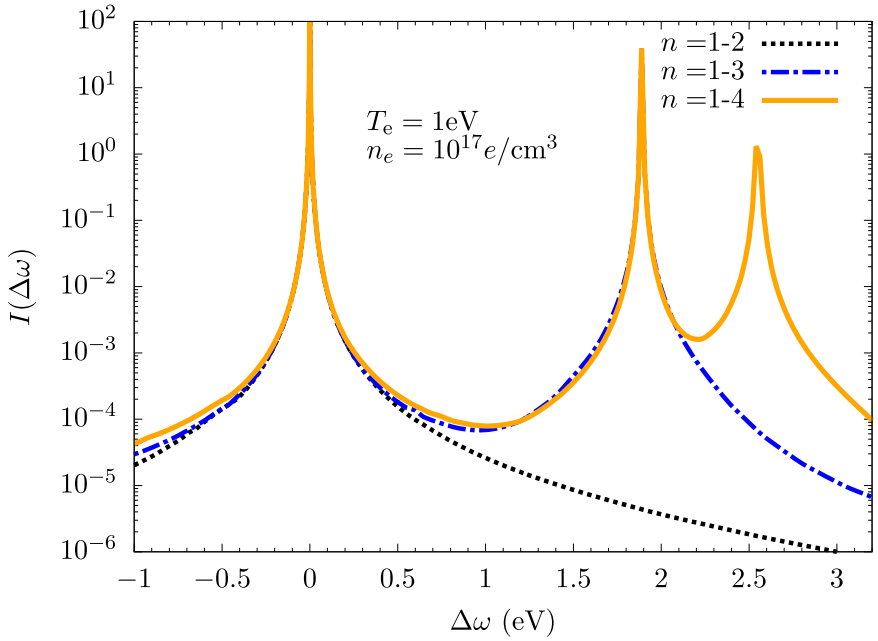

Figure 14. Convergence of the Lyα spectrum with increasing n, but including all dipole moments. The singularities in Figure 13 have disappeared underneath the profiles, and only slight asymmetries are to be seen in the Lyβ and Lyγ lines. The final spectrum, therefore, has no negative points when all dipole moments are included.

Despite the oscillatory behavior as the basis set is increased, integrated quantities do converge. In our calculations, we found that the scattered wave (Equation (A21)) does indeed converge as the basis set increases (even for off-shell scattered waves). And indeed, we see convergence in the line profile, and the wild oscillatory behavior is not seen such that there is a clear trend toward convergence. This is the expected behavior, and has been seen previously in I. Bray & A. T. Stelbovics (1995). Due to unitarity of the close-coupling formalism, convergence in the elastic amplitude ensures convergence in the total cross section via the optical theorem. This, in turn, means convergence in the total excitation and the total integrated ionization cross sections. Accordingly, any integrated parameters converge much quicker than individual components, including K-matrix elements. This is demonstrated in the Lyα profiles in Figure 13, where we show the evolution of the line shapes as more states are added. There are increases in the broadening of the line wings, but the amount of increase decreases with each n added to the calculation. One of the features seen when adding new states is what looks to be a singularity at the Lyβ and Lyγ transitions. Here, what is referred to as the Lyα profile goes negative. This behavior is expected and simply reflects the mixing between different transitions as the density increases. What this ultimately does to the final spectrum is add some asymmetries to the Lyβ and Lyγ transitions; the final line shape when these transitions are added back in will *not* be negative. The size of the asymmetries in the Lyα profile depends on the strength of the neighboring transitions. Therefore, the size of features in the blue wing of the profile will be different for emission and absorption profiles, which is due to the differing populations of the upper and lower states, respectively. The fact that these features have negative points in the isolated Lyα line shape does *not* translate into the final spectrum when all dipole moments are included as demonstrated in Figure 14.

Appendix B
Capturing the Transient Ages of Electron Collisions

The form of Equation (5) is valid for the line center. However, this form is not complete for the wings. U. Fano (1963) points out that there are additional terms that account for the transient effects of the collision (i.e., the line wings). The complete expression for the broadening operator can be derived straightforwardly by writing the frequency evolution of the dipole operator as a convolution of upper and lower states. These additional terms are given by

$$
\begin{aligned}
M_{\text{transient}}(\omega) = \frac{1}{2}\Bigg\{ & -\frac{T(E_l)T^*(E_l-\omega) - T(E_r)T^*(E_r-\omega}{E_l - E_r} \\
& + \frac{T(E_l^*+\omega)T^*(E_r^*) + T(E_r^*+\omega)T^*(E_r^*)}{E_l^* - E_r^*} \\
& + \text{p.v.}\frac{T(E_l)T^*(E_l-\omega) + T(E_r^*+\omega)T^*(E_r^*)}{E_l - \omega - E_r^*} \\
& - \text{p.v.}\frac{T(E_l^*+\omega)T^*(E_l^*) - T(E_r)T^*(E_r-\omega)}{E_l^* + \omega - E_r}\Bigg\} \\
& + \frac{\text{p.v.}}{2\pi i}\int_{-\infty}^{\infty} d\psi \left[\frac{1}{\psi - E_l} - \frac{1}{\psi - \omega - E_l^*}\right] \\
& \times \left[\frac{1}{\psi - E_r} - \frac{1}{\psi - \omega - E_r^*}\right] T(\psi)T^*(\psi - \omega). \qquad \text{(B1)}
\end{aligned}
$$

This final term is equivalent to the terms

$$
\begin{aligned}
& \frac{g(E_l) - g(E_r)}{E_l - E_r} + \frac{g(E_l^*+\omega) - g(E_r^*+\omega)}{E_l^* - E_r^*} \\
& - \frac{g(E_l) - g(E_r^*+\omega)}{E_l - \omega - E_r^*} - \frac{g(E_l^*+\omega) - g(E_r)}{E_l^* + \omega - E_r} \qquad \text{(B2)}
\end{aligned}
$$

given in Equation (55) of U. Fano (1963), where

$$g(E) = \frac{1}{\pi i}\int_{-\infty}^{\infty} d\psi \frac{\text{p.v.}}{\psi - E} T(\psi + i0)T^*(\psi - \omega - i0). \tag{B3}$$

The energies with the subscripts denote which side of the T-matrix the Hamiltonian operator acts on, with the star superscript denoting the lower state. Numerical tests on the final term of Equation (B1), using the form as written or with Equation (B2), show that they give the same answer, although the expression in Equation (B1) is more numerically stable.

B.1. Changes from Fano's Expression

We note that our definition for the last of the transient terms is different from the definition given in U. Fano (1963) by a factor of 2. In a rederivation, we found that the presence of the factor of 2 is in error, having already been factored out of the brackets. Equation (20) is derived from performing an integral over ψ:

$$\frac{1}{2\pi i}\int_{-\infty+i\eta}^{\infty+i\eta} d\psi \left[\frac{1}{\psi - H_0} - \frac{1}{\psi - \omega - H_0^*}\right] \times T(\psi)T^*(\psi - \omega)\left[\frac{1}{\psi - H_0} - \frac{1}{\psi - \omega - H_0^*}\right]. \tag{B4}$$

Here, small imaginary parts for *both* ψ and ω are implied. The two quantities in brackets can be further simplified by taking the eigenvalue depending on whether the Hamiltonian operates on the left side, l, or right side, r, of the T-matrices,[13]

$$\begin{aligned}&\left[\frac{1}{\psi - E_l} - \frac{1}{\psi - \omega - E_l^*}\right]\left[\frac{1}{\psi - E_r} - \frac{1}{\psi - \omega - E_r^*}\right]\\ &= \frac{1}{E_l - E_r}\left[\frac{1}{\psi - E_l} - \frac{1}{\psi - E_r}\right] + \frac{1}{E_l^* - E_r^*}\\ &\times\left[\frac{1}{\psi - \omega - E_l^*} - \frac{1}{\psi - \omega - E_r^*}\right]\\ &- \frac{1}{E_l - \omega - E_r^*}\left[\frac{1}{\psi - E_l} - \frac{1}{\psi - \omega - E_r^*}\right]\\ &- \frac{1}{E_l^* + \omega - E_r}\left[\frac{1}{\psi - \omega - E_l^*} - \frac{1}{\psi - E_r}\right],\end{aligned} \tag{B5}$$

where the final expression is obtained by taking the limit that the small imaginary parts of ψ and ω, η, and ϵ, respectively, are taken to zero:

$$\eta = \Im\psi \to 0^+ \quad \epsilon = \Im\omega \to 0^+ \quad \eta - \epsilon = \Im(\psi - \omega) \to 0^-. \tag{B6}$$

This is accomplished with the relationships

$$\lim_{\eta\to 0}\frac{1}{\psi + i\eta - E_r} = \frac{\text{p.v.}}{\psi - E_r} - i\pi\delta(\psi - E_r), \tag{B7}$$

and

$$\lim_{\epsilon\to 0}\lim_{\eta\to 0}\frac{1}{\psi + i\eta - \omega - i\epsilon - E_r^*} = \frac{\text{p.v.}}{\psi - \omega - E_r^*} + i\pi\delta(\psi - \omega - E_r^*). \tag{B8}$$

We repeat a note by U. Fano (1963), where the quantities such as $(E_r - E_l)^{-1}$ contain no small imaginary part. However, terms such as $(E_l - \omega - E_r^*)^{-1}$ do contain a small imaginary part, i.e., ϵ, and will therefore have real and imaginary components when the limit $\epsilon \to 0$ is taken.

B.2. Implementation

The broadening terms in Equation (9) are relatively straightforward to evaluate. The evaluation of the first four terms of Equation (20) is less straightforward, requiring a 2D integral as well as the evaluation of the energy parameter.

The thermally averaged operator is denoted in the main text by $\mathcal{H}(\omega)$. For the purposes of the discussion below, we will denote the transient terms by $\mathcal{H}_T(\omega)$, which is made up of the various terms,

$$\begin{aligned}\mathcal{H}_T(\omega) = \mathcal{H}_T^{(1)}(\omega) + \mathcal{H}_T^{(2)}(\omega) + \mathcal{H}_T^{(3)}(\omega)\\ + \mathcal{H}_T^{(4)}(\omega) + \mathcal{H}_T^{(5)}(\omega),\end{aligned} \tag{B9}$$

which are the thermal average of the respective terms in Equation (20).

The procedure we used here was to integrate over the variable that was not part of the energy parameter, saving the interpolation for a later step. For example, for

$$\mathcal{H}_T^{(1)}(\omega) = -\frac{1}{2}\left\{\frac{T(E_l)T^*(E_l - \omega)}{E_l - E_r} - \frac{T(E_r)T^*(E_r - \omega)}{E_l - E_r}\right\}_{Av}, \tag{B10}$$

the evaluation of the first term is best done by performing the integral over the state on the right:

$$\Upsilon^{(1,1)}_{aa';bb'}(k_1, \psi) = -\frac{1}{2}\int dk_2 \frac{\langle ak_1|T(E_{ak_1})|a'k_2\rangle\langle bk_1|T(\psi)|b'k_2\rangle}{E_{ak_1} - E_{a'k_2}} e^{-\beta\frac{1}{2}k_2^2}. \tag{B11}$$

Likewise, the second term can be evaluated in a similar manner, but choosing the other perturber coordinate to integrate first,

$$\Upsilon^{(1,2)}_{aa';bb'}(k_2, \psi) = e^{-\beta\frac{1}{2}k_2^2}\frac{1}{2}\int dk_1 \frac{\langle ak_1|T(E_{a'k_2})|a'k_2\rangle\langle bk_1|T(\psi)|b'k_2\rangle}{E_{ak_1} - E_{a'k_2}}, \tag{B12}$$

[13] A sign error in Equation (53) of U. Fano (1963) has been rectified here, although we note that the sign error did not carry into Equation (55) of U. Fano (1963).

thus making the evaluation of the first term

$$[\mathcal{H}_T^{(1)}(\omega)]_{aa';bb'} = n_e \lambda_T^3 \left[\int dk_1 \Upsilon^{(1,2)}_{aa';bb'}(k_2, E_{a'k_2} - \omega) - \int dk_1 \Upsilon^{(1,1)}_{aa';bb'}(k_1, E_{ak_1} - \omega) \right]. \tag{B13}$$

This procedure can be used to efficiently evaluate the first four terms of Equation (20).

The evaluation of the last term of Equation (20) is more involved. The first item to be addressed is that, when exchange is included, the T-matrices (discussed in Appendix A) do not go to zero as $|\psi|$ becomes large; this is because V contains a term that also depends on ψ (e.g., I. Bray & A. T. Stelbovics 1992, where it was labeled as E), meaning that the T-matrix is linear with ψ (Equation (A25)).

Since we have two factors of T within $g(E)$ and then a factor of ψ in the denominator, the total function scales as ψ as $|\psi|$ becomes large; this is numerically undesirable. An examination of Equation (48) in U. Fano (1963) shows that, for the interference terms, the integral converges as ψ^{-4} (not including the factor of ψ^2 in the T-matrices). Therefore, when evaluating all the factors in that integral, including the T-matrices should converge as ψ^{-2}. Rather than evaluating each individual $g(E)$, we evaluate the total expression as given in Equation (20), where the contribution to the broadening is

$$\mathcal{H}_T^{(5)}(\omega) = \frac{\text{p.v.}}{2\pi i} \int d\psi \iint dk_1 dk_2 \left[\frac{1}{\psi - E_{ak_1}} - \frac{1}{\psi - \omega - E_{bk_1}} \right] \left[\frac{1}{\psi - E_{a'k_2}} - \frac{1}{\psi - \omega - E_{b'k_2}} \right] \times \langle ak_1 | T(\psi) | a'k_2 \rangle \langle bk_1 | T^*(\psi - \omega) | b'k_2 \rangle e^{-\beta \frac{1}{2} k_2^2}. \tag{B14}$$

Here, the integrals over k_1 and k_2 are performed first, using the technique in Equation (A28), then the final integral over ψ is performed last.

This final term of the broadening operator is the more numerically stable form compared to the form presented in the original U. Fano (1963) work. The reason for this is that this form has an appropriate cancellation of terms. One of the main challenges with evaluating the final term of the broadening operator is that, as the T-matrices become large, they become linear in ψ; see Equation (A25).

The grid of ψ that we choose is not uniform; we concentrate points in areas of interest, such as thresholds and H^- resonances. This can cause a number of undersamplings or oversamplings of the singularities in Equation (B14). However, when there is a singularity, such as around resonances, $T(\psi)$ needs to be properly sampled in the integral of Equation (B14). If the singularities that appear in the T-matrix, such as those around resonances, are poorly sampled, the integral will not cancel as it should. Further, if one of the $(\psi - E)^{-1}$ factors is not properly sampled, the integral will no longer go to zero around featureless points, nor properly capture when it lines up with a T-matrix singularity. Therefore, we make a grid of ψ' (the prime is used to distinguish the integral evaluated in Equation (B14) versus the grid used to evaluate the T-matrices), which is a shifted grid of $\psi' = \psi - \omega$. This ensures that the singularities are well sampled and cancel appropriately.

The calculation of Equation (B14) is further complicated by the real part of the solution trying to capture the H^- ground state, $1s^2\ ^1S$, and the excited state, $2p^2\ ^3P^e$. These H^- states are bound and thus have no imaginary component; therefore, $\Re T(\psi)$ is singular in the vicinity of these energies. This can pose problems evaluating Equation (B14) numerically that are unique to these states of H^-; all other states of H^- are autoionizing and have some width to them, meaning that they are not singular as $\psi - E_{H^-} \Rightarrow 0$. Therefore, the exact numerical evaluation of Equation (B14) is dependent on the sampling of points in ψ around E_{1s^2} and E_{2p^2} and is sensitive to the choice of k-grid, as the k-grid causes slight changes in the positions of these singularities. As stated above, this only applies to thermal averages that involve the ^1S and the $^3P^e$ angular momentum states. The way around this is, for these particular spin and angular momentum states, we assign a small imaginary part to the energy that removes the singular nature of the states. This creates an additional case for the numerical weights for the Green's function described above:

$$w(k_j) = \begin{cases} \frac{1}{|q|}\left(\ln \left| \frac{q + (k_j + k_{j+1})/2}{q - (k_j + k_{j+1})/2} \right| - \ln \left| \frac{q + (k_j + k_{j-1})/2}{q - (k_j + k_{j-1})/2} \right| \right) & \text{if} \quad q^2 > 0 \\ \frac{2}{(k_j + k_{j+1})/2} - \frac{2}{(k_j + k_{j-1})/2} & \text{if} \quad q^2 = 0 \\ \frac{2}{|q|}(\arctan((k_j + k_{j+1})/2|q|) - \arctan((k_j + k_{j-1})/2|q|)) & \text{if} \quad q^2 < 0 \\ \frac{2}{\sqrt{-2q^2 - i2\eta}} \left[\arctan\left(\frac{k_j + k_{j+1}}{\sqrt{-2q^2 - i2\eta}} \right) - \arctan\left(\frac{k_j + k_{j-1}}{\sqrt{-2q^2 - i2\eta}} \right) \right] & \text{if} \quad q^2 < \min\left(E_i + \frac{1}{2}k^2 \right)_{\Pi LS}, \end{cases} \tag{B15}$$

where, in this last case, the energy in the Green's function has to be less than the minimum energy of the eigenstates in that ΠLS, which in the case of ^1S would be -0.5 hartree, and in the case of $^3P^e$ is -0.125 hartree.

ORCID iDs

Thomas A. Gomez https://orcid.org/0000-0001-8748-5466
Mark C. Zammit https://orcid.org/0000-0003-0473-379X
Jackson R. White https://orcid.org/0000-0003-4052-2746
Evgeny Stambulchik https://orcid.org/0000-0002-7100-8793
Igor Bray https://orcid.org/0000-0001-7554-8044

Christopher J. Fontes https://orcid.org/0000-0003-1087-2964
Michael H. Montgomery https://orcid.org/0000-0002-6748-1748
Bart H. Dunlap https://orcid.org/0000-0003-0181-2521
Donald E. Winget https://orcid.org/0000-0003-0181-2521

References

Alexiou, S. 2009, HEDP, 5, 225
Alexiou, S., & Lee, R. W. 2006, JQRST, 99, 10
Allard, N. F., Hébrard, G., Dupuis, J., et al. 2004, ApJL, 601, L183
Allard, N. F., Kielkopf, J., Drira, I., & Schmelcher, P. 2000, EPJD, 12, 263
Allard, N. F., Royer, A., Kielkopf, J. F., & Feautrier, N. 1999, PhRvA, 60, 1021
Baranger, M. 1958a, PhRv, 112, 855
Baranger, M. 1958b, PhRv, 111, 481
Baranger, M. 1958c, PhRv, 111, 494
Bergeron, P., Saffer, R. A., & Liebert, J. 1992, ApJ, 394, 228
Bergeron, P., Wesemael, F., Lamontagne, R., et al. 1995, ApJ, 449, 258
Bethe, H. A., & Salpeter, E. E. 1957, Quantum Mechanics of One- and Two-electron Atoms (New York: Academic)
Bhatia, A. K., & Temkin, A. 1969, PhRv, 182, 15
Bhatia, A. K., Temkin, A., & Perkins, J. F. 1967, PhRv, 153, 177
Bischoff-Kim, A., Montgomery, M. H., & Winget, D. E. 2008, ApJ, 675, 1512
Boercker, D. B., & Iglesias, C. A. 1984, PhRvA, 30, 2771
Boercker, D. B., Iglesias, C. A., & Dufty, J. W. 1987, PhRvA, 36, 2254
Bohlin, R. C., Hubeny, I., & Rauch, T. 2020, AJ, 160, 21
Bohm, D., & Gross, E. P. 1949a, PhRv, 75, 1851
Bohm, D., & Gross, E. P. 1949b, PhRv, 75, 1864
Bray, A. W., Abdurakhmanov, I. B., Kadyrov, A. S., Fursa, D. V., & Bray, I. 2015, CoPhC, 196, 276
Bray, A. W., Abdurakhmanov, I. B., Kadyrov, A. S., Fursa, D. V., & Bray, I. 2016, CoPhC, 203, 147
Bray, A. W., Abdurakhmanov, I. B., Kadyrov, A. S., Fursa, D. V., & Bray, I. 2017, CoPhC, 212, 55
Bray, I., & Stelbovics, A. T. 1992, PhRvA, 46, 6995
Bray, I., & Stelbovics, A. T. 1995, CoPhC, 85, 1
Bylicki, M., & Bednarz, E. 2003, PhRvA, 67, 022503
Calisti, A., Khelfaoui, F., Stamm, R., Talin, B., & Lee, R. W. 1990, PhRvA, 42, 5433
Capes, H., & Voslamber, D. 1972, PhRvA, 5, 2528
Chandrasekhar, S. 1944, ApJ, 100, 176
Cho, P. B., Gomez, T. A., Montgomery, M. H., et al. 2022, ApJ, 927, 70
Djurović, S., Ćirišan, M., Demura, A. V., et al. 2009, PhRvE, 79, 046402
Drake, G. W. 1970, PhRvL, 24, 126
Dupuis, J., Vennes, S., Bowyer, S., Pradhan, A. K., & Thejll, P. 1995, ApJ, 455, 574
Dzierżęga, K., Sobczuk, F., Krehlik, T., & Stambulchik, E. 2024, PhRvE, 109, 065214
Fano, U. 1963, PhRv, 131, 259
Fontaine, G., Brassard, P., & Bergeron, P. 2001, PASP, 113, 409
Frommhold, L. 1993, Collision-induced Absorption in Gases (New York: Cambridge Univ. Press)
Gigosos, M. A., & Cardenoso, V. 1987, JPhB, 20, 6005
Gomez, T. A., Nagayama, T., Cho, P. B., et al. 2021, PhRvL, 127, 235001
Gomez, T. A., Nagayama, T., Cho, P. B., et al. 2022, JPhB, 55, 034002
Gomez, T. A., Nagayama, T., Fontes, C. J., et al. 2020, PhRvL, 124, 055003
Gomez, T. A., Nagayama, T., Kilcrease, D. P., Montgomery, M. H., & Winget, D. E. 2016, PhRvA, 94, 022501
Gomez, T. A., Nagayama, T., Kilcrease, D. P., Montgomery, M. H., & Winget, D. E. 2018, PhRvA, 98, 012505
Gomez, T. A., Stambulchik, E., & White, J. 2024, PhRvA, 109, 052804
Gordon, K. D., Bohlin, R., Sloan, G. C., et al. 2022, AJ, 163, 267
Griem, H. R. 1974, Spectral Line Broadening By Plasmas (New York: Academic)
Griem, H. R., Blaha, M., & Kepple, P. C. 1979, PhRvA, 19, 2421
Griem, H. R., Kolb, A. C., & Shen, K. Y. 1959, PhRv, 116, 4
Griem, H. R., Ralchenko, Y. V., & Bray, I. 1997, PhRvE, 56, 7186
Hannachi, I., Stamm, R., Rosato, J., & Marandet, Y. 2023, AdSpR, 71, 1269
Hubeny, I., Allende Prieto, C., Osorio, Y., & Lanz, T. 2021, arXiv:2104.02829
Hubeny, I., & Lanz, T. 1995, ApJ, 439, 875
Hubeny, I., & Mihalas, D. 2014, Theory of Stellar Atmospheres (Princeton, NJ: Princeton Univ. Press)
Hussey, T., Dufty, J. W., & Hooper, C. F. 1975, PhRvA, 12, 1084
Hussey, T. W., Dufty, J. W., & Hooper, C. F. J. 1977, PhRvA, 16, 1248
Iglesias, C. A. 2016, HEDP, 18, 14
Iglesias, C. A., & Gomez, T. A. 2024, HEDP, 50, 101080
Junkel, G. C., Gunderson, M. A., Hooper, C. F. J., & Haynes, D. A. J. 2000, PhRvE, 62, 5584
Jura, M. 2003, ApJL, 584, L91
Kalirai, J. S., Hansen, B. M. S., Kelson, D. D., et al. 2008, ApJ, 676, 594
Kepple, P., & Griem, H. R. 1968, PhRv, 173, 317
Kielkopf, J. F., & Allard, N. F. 1998, PhRvA, 58, 4416
Kielkopf, J. F., Allard, N. F., & Huber, J. 2004, ApJL, 611, L129
Kilcrease, D. P., Mancini, R. C., & Hooper, C. F. J. 1993, PhRvE, 48, 3901
Kolb, A. C., & Griem, H. 1958, PhRv, 111, 514
Kowalski, P. M., & Saumon, D. 2006, ApJL, 651, L137
Kraus, B. F., Gao, L., Hill, K. W., et al. 2021, PhRvL, 127, 205001
Lehner, N., Jenkins, E. B., Gry, C., et al. 2003, ApJ, 595, 858
Lemke, M. 1997, A&AS, 122, 285
Lippmann, B. A., & Schwinger, J. 1950, PhRv, 79, 469
Nagayama, T., Bailey, J. E., Mancini, R. C., et al. 2016, HEDP, 20, 17
Narayan, G., Matheson, T., Saha, A., et al. 2019, ApJS, 241, 20
O'Brien, J. T., & Hooper, C. F. J. 1974, JQSRT, 14, 479
Rau, A. R. P. 1996, JApA, 17, 113
Rosato, J. 2017, HEDP, 22, 60
Rosato, J., Marandet, Y., & Stamm, R. 2020, JQSRT, 249, 107002
Roszman, L. J. 1975, PhRvL, 34, 785
Sahu, S., Gänsicke, B. T., Tremblay, P.-E., et al. 2023, MNRAS, 526, 5800
Sampson, D. H., Zhang, H. L., & Fontes, C. J. 2009, PhR, 477, 111
Saumon, D., Blouin, S., & Tremblay, P.-E. 2022, PhR, 988, 1
Saumon, D., Holberg, J. B., & Kowalski, P. M. 2014, ApJ, 790, 50
SLSP 2024, Spectral Line Shapes in Plasmas Workshop (Rehovot: Weizmann Inst. of Science), https://plasma-gate.weizmann.ac.il/slsp/
Smith, E. W., Cooper, J., & Vidal, C. R. 1969, PhRv, 185, 140
Sobczuk, F., Dzierżęga, K., & Stambulchik, E. 2022, PhRvE, 106, L023202
Stambulchik, E. 2013, HEDP, 9, 528
Stambulchik, E., Fisher, D. V., Maron, Y., Griem, H. R., & Alexiou, S. 2007, HEDP, 3, 272
Stambulchik, E., & Iglesias, C. A. 2022, PhRvE, 105, 055210
Stambulchik, E., & Maron, Y. 2006, JQSRT, 99, 730
Stehle, C., & Jacquemot, S. 1993, A&A, 271, 348
Stelbovics, A. T. 1990, PhRvA, 41, 2536
Stelbovics, A. T., & Bransden, B. H. 1989, JPhB, 22, L451
Tighe, R. J., & Hooper, C. F. J. 1976, PhRvA, 14, 1514
Tremblay, P. E., & Bergeron, P. 2009, ApJ, 696, 1755
Tremblay, P.-E., Fontaine, G., Fusillo, N. P. G., et al. 2019, Natur, 565, 202
Tremblay, P. E., Ludwig, H. G., Steffen, M., Bergeron, P., & Freytag, B. 2011, A&A, 531, L19
van Horn, H. M. 1968, ApJ, 151, 227
Van Horn, H. M. 2015, Unlocking the Secrets of White Dwarf Stars (Cham: Springer)
Vidal, C. R., Cooper, J., & Smith, E. W. 1973, ApJS, 25, 37
Wiese, W. L., Kelleher, D. E., & Paquette, D. R. 1972, PhRvA, 6, 1132
Williams, K. A., Bolte, M., & Koester, D. 2009, ApJ, 693, 355
Winget, D. E., Hansen, C. J., Liebert, J., et al. 1987, ApJL, 315, L77
Winget, D. E., Sullivan, D. J., Metcalfe, T. S., Kawaler, S. D., & Montgomery, M. H. 2004, ApJL, 602, L109
Woltz, L. A., & Hooper, C. F. J. 1984, PhRvA, 30, 468
Wood, B. E., Redfield, S., Linsky, J. L., Müller, H.-R., & Zank, G. P. 2005, ApJS, 159, 118
Zuckerman, B., Koester, D., Melis, C., Hansen, B. M., & Jura, M. 2007, ApJ, 671, 872
Zammit, M. C., Fursa, D. V., & Bray, I. 2010, PhRvA, 82, 052705